university of groningen

faculty of science and engineering

Master's Thesis

May 16, 2024

Charge transfer in low energy Sn^{4+} collisions with molecular hydrogen

---

Lennart Tinge

s3820734

First examiner
prof. dr. ir. R. Hoekstra
Second examiner
prof. dr. S. Hoekstra
Daily supervisors
E. de Wit
K. Bijlsma

Abstract

An important step in the production of advanced computer chips is facilitated by the EUV nanolithography machines from ASML. In these machines, EUV light is produced by shooting a tin droplet with a highly powered laser, creating a laser produced plasma (LPP). The plasma emits the EUV light required for nanolithography and is collected and focused by costly, atomically flat mirrors. The debris left behind from the LPP may consist in part of energetic, highly charged tin ions which can potentially damage the mirrors. By introducing a buffer gas of H_2, the ions are slowed down via collisions and the charge state is reduced via charge transfer with the gas. In order to gain more general insight into electron capture processes, charge transfer cross sections for Sn^{4+} with a kinetic energy ranging from 1 keV to 16 keV colliding with H_2 gas are experimentally determined in this work. This is done at the Zernike low energy ion facility (ZERNIKELEIF). After collisions with hydrogen, ionic populations, from the now multiply charged ion beam, are measured with a gridless retarding field analyser (RFA). From these measurements, the charge transfer cross sections are determined. It was found that cross sections for single electron capture for Sn^{4+} are significantly smaller than for Sn^{3+}, which is likely due to the difference in availability of quantum states for the electron to be captured into. The charge transfer cross sections for double electron capture were found to be larger for Sn^{4+} than for Sn^{3+}. Additionally, the experimental results are compared to calculations from the Landau-Zener model of charge exchange. Finally, the potential presence of excited metastable Sn^{4+} ions in the ion beam is discussed as well as their influence on determined cross sections.

Contents

1 Introduction

In recent years, the demand for computing power has increased significantly, especially due to the growth of data centres and artificial intelligence. This demand is expected to grow even more and with it, the corresponding energy consumption. In order to keep up with this demand, it is necessary for computer chips to become more powerful, while energy consumption is decreased. Further miniaturization of transistors inside computer chips allows for faster computations, while also decreasing the energy consumption. However, this requires increasingly complex machines. Currently, production of some of the most advanced computer chips is enabled by ASML's extreme ultraviolet light (EUV) nanolithography machines. These machines use a laser produced plasma (LPP) to generate the EUV light required to perform nanolithography on the wafers, which is an important step in the process of producing chips. The small wavelength EUV light is crucial to the production of the computer chips, since smaller wavelengths allow for smaller structures to be printed on the wafers. In order to produce the EUV light, a tin droplet is turned into a plasma by absorption of infrared radiation fired by a powerful laser. The highly charged tin ions in the plasma then emit electromagnetic radiation with a range of wavelengths, including the required EUV light with a wavelength of 13.5 nm. Since most materials absorb EUV radiation, the EUV light needs to be transported through a vacuum and multiple atomically flat mirrors are used to reflect and shape the light. These multilayer mirrors are specifically designed for use in the EUV nanolithography machines. Inside the chamber where the EUV light is produced, a collector mirror reflects the emitted light towards the next mirror. When the LPP is produced, the collector mirror is exposed to energized highly charged tin ions, if no precautions are taken. In order to protect the collector mirror from this debris, a buffer gas of molecular hydrogen is introduced into the plasma chamber. During collisions with the tin ions and the hydrogen molecules, the tin ions lose kinetic energy as well as capture electrons from the hydrogen. In this work, the focus lies on charge transfer from the molecular hydrogen to tin ions. In order to optimize the protection of the collector mirror, it is important to understand the process of charge transfer and how exactly a tin ion is neutralized by the hydrogen buffer gas. A piece of this puzzle is the determination of charge transfer cross sections, which represent probabilities for a certain charge transfer process to take place for a given charged tin ion. In this thesis, measurements were performed at the Zernike Low Energy Ion Facility (ZERNIKELEIF) on collisions of Sn^{4+} with molecular hydrogen using a gridless retarding field analyser (RFA). First, characterisation measurements of the RFA and the tin oven were performed. Then, the presence of a contamination ion in the ion source for cross section measurements of ^{120}Sn^{4+} is analysed. Afterwards, charge populations were determined using an RFA after collisions of a ^{118}Sn^{4+} ion beam with molecular hydrogen. From these measurements, charge transfer cross-sections were determined using an extrapolation into the limit of a single collision regime. The results are interpreted in the reference frame of the classical overbarrier model of charge transfer. Additionally, the results are compared to multichannel calculations from the Landau-Zener approximation. On the basis of these results, the potential presence of meta stable Sn^{4+} ions is discussed.

2 Theory of charge transfer and atomic collisions

Atomic collisions can be divided into elastic collisions and inelastic collisions. In elastic collisions, the internal energy of the involved particles does not change, but the incident particle can be deflected by a certain angle. In figure 2.1, an atomic collision between an ion and a neutral atom can be seen. The impact parameter b is indicated, which is the initial distance between the projectile and target in the direction perpendicular to the direction of momentum. In inelastic collisions, a change in electronic energy occurs, which can happen via two processes. For an incident atom A colliding with a target atom B, energy can be transferred such that one or both atoms are now in an excited state:

$$A + B \to A + B^* \tag{2.1}$$

In this process, atom A loses some of its kinetic energy. In the other process, charge transfer occurs. For a charged particle A, multiple charge transfer processes can occur. For a tin ion colliding with hydrogen, the most important processes are the following:

$$\mathrm{Sn}^{q+} + \mathrm{H}_2 \to \mathrm{Sn}^{(q-1)+} + \mathrm{H}_2^+ \qquad \text{Single electron capture} \tag{2.2}$$

$$\mathrm{Sn}^{q+} + \mathrm{H}_2 \to \mathrm{Sn}^{(q-2)+} + 2\mathrm{H}^+ \qquad \text{Bound double capture} \tag{2.3}$$

$$\mathrm{Sn}^{q+} + \mathrm{H}_2 \to \mathrm{Sn}^{(q-1)+} + 2\mathrm{H}^+ + e^- \qquad \text{Autoionizing electron capture} \tag{2.4}$$

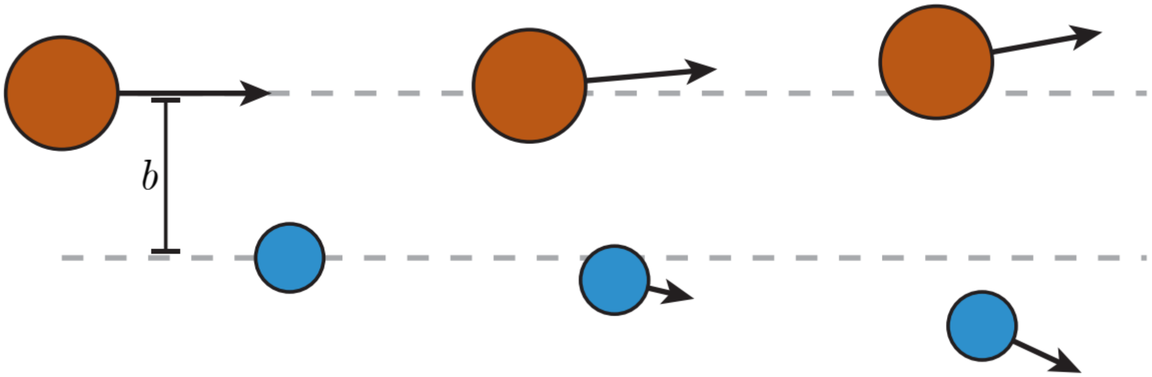

Figure 2.1: Schematic of a collision between a projectile ion and a neutral target, defining the impact parameter b. When the internuclear distance is small enough, the interaction between the projectile and target will cause scattering.

In single electron capture, a single electron is captured from the target atom, while in double capture two electrons are captured from the target atom. In the autoionizing electron capture process, two electrons are captured and one captured electron is ionized from the projectile atom. Different models have been proposed to describe charge transfer. However, many do not fall within the scope of this thesis. Therefore, the classical overbarrier model and the Landau-Zener model are used to describe charge transfer in this thesis.

2.1 Classical overbarrier model

The overbarrier model is a simple classical model describing charge transfer between a projectile ion and a target atom [1]. When the particles are close together, the Stark effect occurs, which is a shift of energy levels of particles, caused by the presence of an external electric field. At some internuclear distance R, the shift in the binding energy of the target atom is described by:

$$E_i = E_{B,i} - \frac{q}{R} \tag{2.5}$$

where $E_{B,i}$ is the unshifted binding energy of electron i and q is the charge on the projectile. The target and projectile have a superimposed potential at an internuclear distance R of:

$$V(x) = -\frac{q}{x} - \frac{1}{R-x} \tag{2.6}$$

where x is the distance between the electron to the projectile. This potential has a maximum value at:

$$V_m = -\frac{(\sqrt{q}+1)^2}{R} \tag{2.7}$$

The overbarrier model assumes that charge transfer takes place when the height of the potential barrier between the two particles equals the Stark shifted binding energy of the electron. This condition is satisfied when equation 2.5 equals equation 2.7:

$$E_B - \frac{q}{R} = -\frac{(\sqrt{q}+1)^2}{R} \tag{2.8}$$

By rearranging this equation, a characteristic internuclear distance R_c can be found at which an electron can be captured from the target atom:

$$R_c = \frac{2\sqrt{q}+1}{E_B} \tag{2.9}$$

Figure 2.2 shows the potential shift of a system of H_2 and Sn^{3+}. When the internuclear separation in a collision between the tin ion and hydrogen molecule decreases, the Coulomb potential of the ion will decrease the potential barrier for the electron on the hydrogen. When the internuclear distance becomes smaller than R_c, the potential barrier is low enough for the electron to transfer to the tin ion. When the internuclear distance increases again, the barrier will increase, but the electron will remain on the tin ion. In the original overbarrier model, charge transfer will always take place when the internuclear distance becomes smaller than R_c. From these assumptions, the cross section for capturing a single electron is then defined as:

$$\sigma = \pi R_c^2 \tag{2.10}$$

It is also possible to extend this model to account for multielectron processes [3]. The equation for the characteristic internuclear distance then becomes:

$$R_i = \frac{2\sqrt{i(q-i+1)}+i}{E_B, i} \tag{2.11}$$

where i indicates which electron of the target is captured, sorted by binding energy. With this extension, the cross section for single capture and processes involving two electrons are determined by:

$$\sigma_1 = \pi(R_1^2 - R_2^2) \tag{2.12}$$
$$\sigma_2 = \pi R_2^2 \tag{2.13}$$

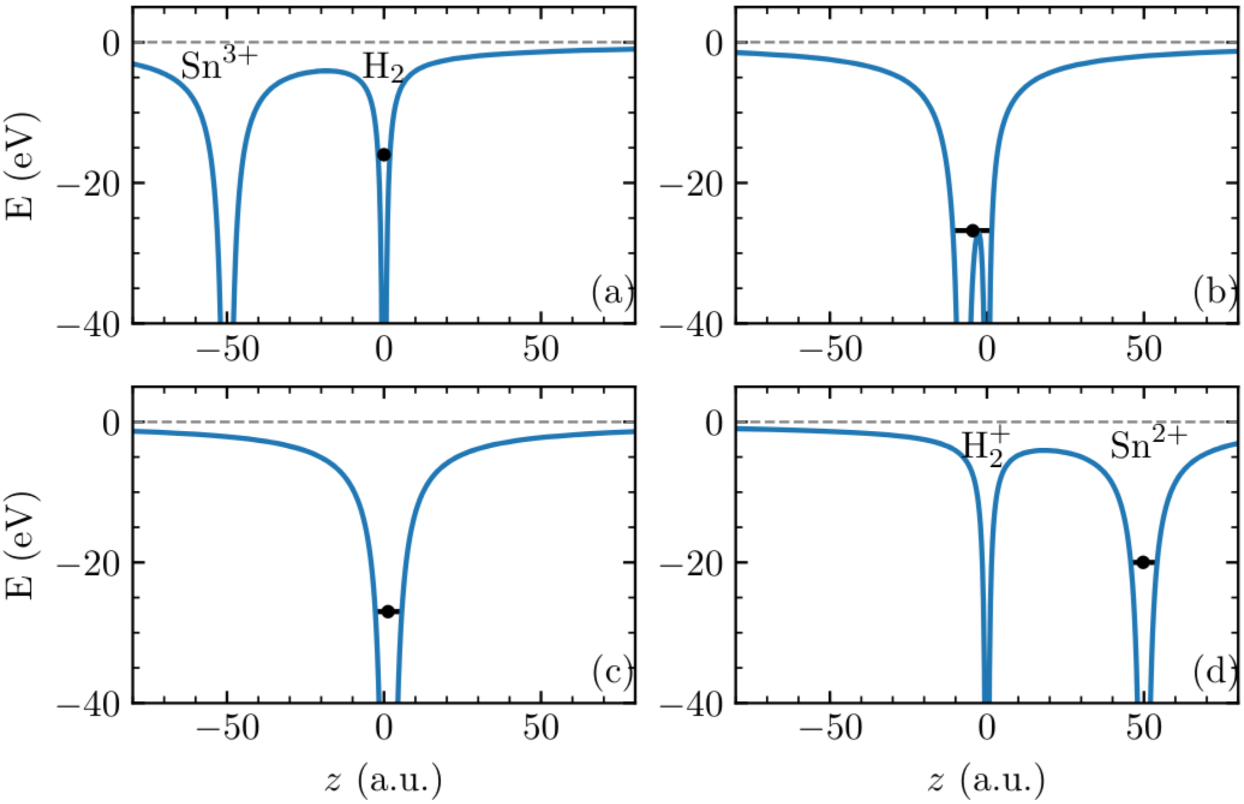

Figure 2.2: Visual representation of charge transfer in the overbarrier model. When a tin ion collides with a hydrogen molecule, the binding energy of the electron is Stark shifted by the Coulomb field of the ion. However, the potential barrier for the electron to transfer to the tin ion is reduced at a higher rate. When the internuclear distance becomes small enough, the electron from the hydrogen will then transfer to the tin ion, where it will stay when the internuclear distance increases again. Image adapted from [2].

In this case, σ_2 is comprised of autoionizing electron capture as well as bound double capture processes. In our experimental determination of cross-sections, autoionizing electron capture contributes to σ_1. Therefore, calculated values of σ_1 and σ_2 will deviate more with experimental results when autoionizing electron capture becomes more prevalent.

The overbarrier model is a very simple model and many aspects of a collision are not taken into account, such as kinetic energy of the projectile and availability of electronic states in the projectile. Furthermore, the overbarrier model assumes electron capture always occurs when the $R < R_c$, which is not realistic. Therefore, overbarrier model calculations often deviate from experimental results. Still, the model can be used as a way to interpret experimental results.

2.2 Landau Zener model

The Landau Zener model is a model that uses crossing points of the potential energy curves of two systems to describe the charge transfer process that can occur [4]. Potential energy curves can be constructed by a number of different potentials. A simple way to model a system of two charged particles is by using a Coulomb potential. For a system with a charged and a neutral particle, the coulomb potential will be zero. To model the potential at very small internuclear distances, a shielded potential such as the Ziegler-Biersack-Littmark (ZBL) potential can be used [5]. In figure 2.3a, potential energy curves for a system with a projectile ion A^{q+} and a target atom B can be seen. The blue curve indicates a neutral system modeled by a ZBL potential and the orange and green curves indicate a system in which charge transfer has occurred from the initial system. The green curve shows a system in some excited state, which does not cross the blue curve of the system, which makes charge transfer impossible in the Landau-Zener model. Since the orange curve does cross the blue curve, charge transfer is possible at the crossing. Considering that the neutral and charged particles are in eigenstates ϕ_1 and ϕ_2 respectively, the state at the crossing can be written down as some linear combination of both states when R changes with some finite velocity:

$$\Phi = A_1(R)\phi_1(x/R) + A_2(R)\phi_2(x/R) \tag{2.14}$$

The Hamiltonian of the individual wavefunctions then become:

$$H\phi_1 = \epsilon_1\phi_1 + \epsilon_{12}\phi_2 \tag{2.15}$$

$$H\phi_2 = \epsilon_{12}\phi_1 + \epsilon_2\phi_2 \tag{2.16}$$

In order to gain an expression for the probability for a transition to occur, some simplifications are made. Firstly, it is assumed that ϵ_{12} is much smaller than the relative kinetic energy of the systems. Because of this, the motion of the particles can be considered as external parameters and R becomes a known function of time. Secondly, it is assumed that the transition region is small enough that ϵ_1 - ϵ_2 is a linear function of time, which is satisfied when ϵ_{12} is sufficiently small. From these assumptions, Zener determined an expression for the probability for a so called diabatic transition:

$$p = e^{\frac{-2\pi H_{12}^2}{v_b \Delta F}} \tag{2.17}$$

where H_{12} is an element of the coupling matrix of the system for one electron capture processes, ΔF is the difference in slope of the potential curves at the crossing and v_b is the radial velocity of the projectile at the crossing, given by:

$$v_b = v(1 - b^2/R_c^2)^{1/2} \tag{2.18}$$

where b is the impact parameter and R_c is the radius at the crossing of the potential curves. After original determination of a generic expression for H_{12} by Olsen et al.[6], several improved descriptions of H_{12} have been made such as by Kimura et al. [7]:

$$H_{12} = 5.48\sqrt{q}\,\text{exp}(-1.324\alpha\sqrt{q}R_c) \tag{2.19}$$

where α = $\sqrt{2I_t}$ and I_t is the ionization potential of the target. The forefactor of 5.48 was chosen by Kimura et al. based on agreement with their results. Based on agreement with results on charge transfer cross section for Sn^{3+}, a forefactor of 5.8 [8] is chosen in this work. Due to the vibrational energy present in the hydrogen molecule, an additonal Franck-Condon factor, FC, owing to the Franck-Condon principle, can be introduced to this equation [6]:

$$H_{12} = 5.8\sqrt{q}\sqrt{FC}\,\text{exp}(-1.324\alpha\sqrt{q}R_c) \tag{2.20}$$

In figure 2.3(b,c,d,e), the possible transitions can be seen. When the internuclear distance first decreases and reaches R_c, a transition is possible. When R increases again and reaches R_c, another transition is possible. A diabatic transition is a transition on which the system follows along the same potential curve after reaching the crossing, while an adiabatic transition is a transition in which the system will follow a new potential curve. Therefore, there are four pathways in total for the collision system to follow. From equation 2.17, the probability for a adiabatic transition simply becomes $1-p$. Since charge transfer occurs when one diabatic and one adiabatic transition has taken place, the probability for charge transfer to occur at some impact parameter b is then:

$$P = 2p(1-p) \tag{2.21}$$

The total cross-section is found by integrating this probability over the impact parameter:

$$\sigma = 2\pi \int Pb\, db \tag{2.22}$$

This model can be expanded to incorporate multiple potential curve crossings. In that case, the total probability of a charge transfer process changes, depending on the number of channels that are added. The cross section is then calculated by equation 2.22 for the total probability for a given impact parameter. In this thesis, it is assumed that adiabatic transitions, and thus charge transfer, only occur at the curve crossings when spin is conserved during the transition. For single electron capture, this would require a singlet state ion to always become a doublet after electron capture, a doublet state ion to become a singlet or quartet and a triplet state ion to become a doublet or a quartet. There is some discussion on how to calculate charge transfer cross sections for double electron capture. The process can be seen as two curve crossings in which a single electron is captured [9], or as a single crossing where two electrons are captured, with some correction factor [10]. In this work, the process is seen as a single curve crossing where two electrons are captured, since this makes the Landau-Zener calculations much less complicated. In this case, spin conservation would require the spin state of the ion to be the same in the initial and final charge state.

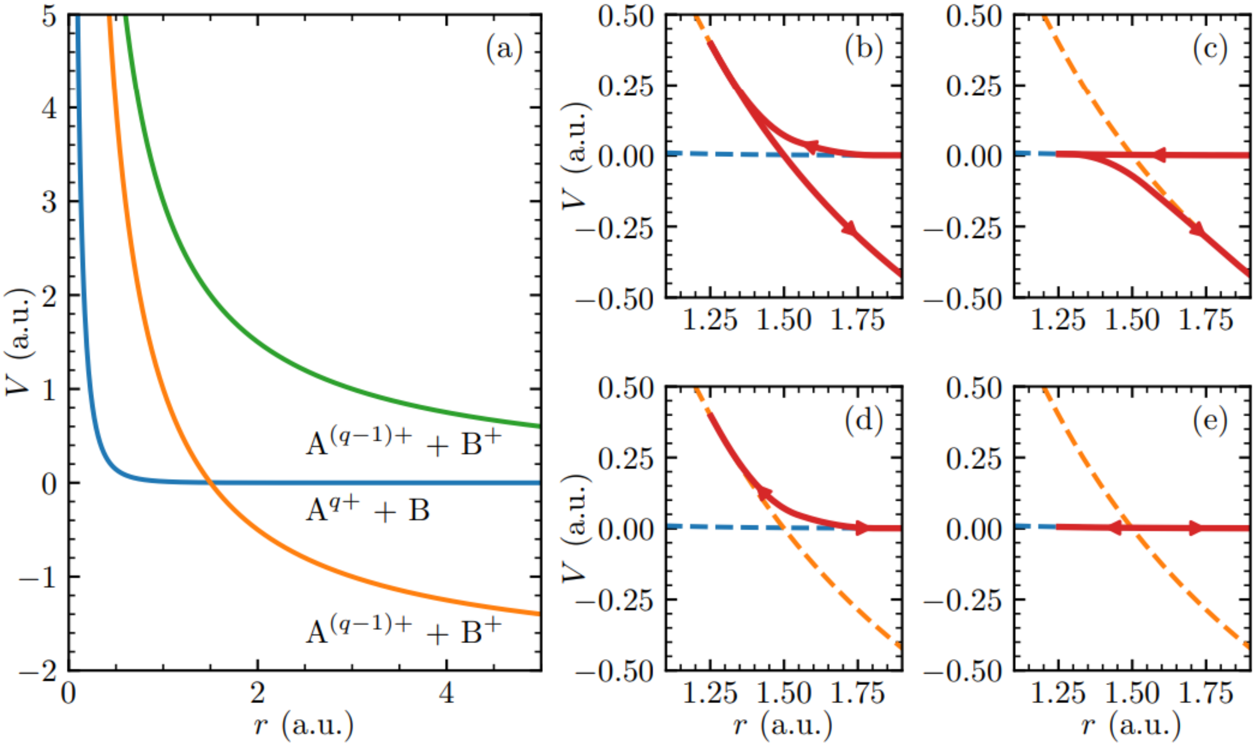

Figure 2.3: Schematic of potential energy curves of three systems of a projectile ion A with target B. The green and orange curve indicate systems in which charge transfer has taken place. The green curve represents a system in which A^{q+} is in an excited state and it does not cross the blue line. The orange line crosses the blue line and at this crossing, charge transfer is possible. At this crossing point, 4 possible transitions can take place, indicated in b, c, d and e.

3 Zernike low energy ion facility

Experiments conducted in this thesis were performed using the Zernike Low Energy Ion-beam Facility (ZERNIKELEIF) at the university of Groningen. In ZERNIKELEIF, low energy ion beams can be created and their interaction with gases or surfaces can be studied. The ion beam is created in an ion source and can be transported to two different experimental setups.

3.1 Ion source

In ZERNIKELEIF, an electron cyclotron resonance ion source (ECRIS) is used for the creation of a plasma, consisting out of different ions. Different gases can be added into the ion source from which a plasma is produced. These gases are usually noble gases, nitrogen or oxygen. Additionally, it is possible to introduce gaseous tin to the source via a tin oven. The tin oven consist of a crucible which can be heated by letting a current run through a tungsten filament around the oven. A small amount of solid tin can be inserted into the oven. By heating the tin oven, tin is evaporated into the ion source. When the tin atoms or other gases are introduced into the source, a strong permanent magnet causes electrons removed from the ions inside

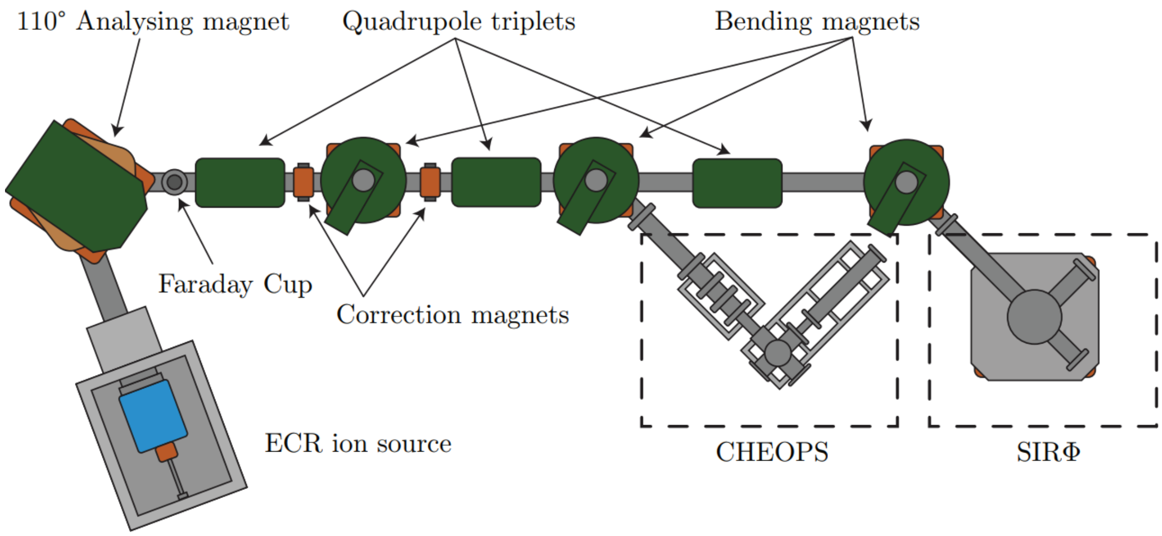

Figure 3.1: Schematic of ZERNIKE-LEIF. Ions are created in the ECR ion source and can be transported towards the experimental setup of CHEOPS, where ion-gas interactions are studied or to SIRΦ where ion-surface interactions are studied.

to perform a cyclotron motion. The angular frequency of this motion is given by:

$$\omega_c = \frac{e|B|}{m_e} \tag{3.1}$$

where e is the elementary charge, B the strength of the magnetic field and m_e the mass of the electron. By absorption of radio frequency (RF) which is resonant with the frequency of the cyclotron motion, the electrons are accelerated such that they have enough energy to ionize the gas in the ion source. This creates a plasma with ions of different charge states. The entire ion source is placed at a high positive voltage of V_{source}, which causes the ions to experience a potential difference between the source and the beamline. This potential difference causes the ions to move from the higher to the lower potential. This gives them a kinetic energy in eV depending on the charge state of the ion:

$$E_{kin} = q(V_{source} + V_{plasma}) \tag{3.2}$$

where V_{plasma} is the intrinsic plasma potential. Typically, the plasma potential is negligibly small compared to the potential put on the ion source. Additionally, it is possible to place a negative voltage to puller electrodes placed on the outside of the ion source. This causes the ions in the ion source to experience a larger potential difference, allowing for the extraction of more ions from the source. After extraction of the ions from the source, an einzel lens can be used to focus the ion beam. The ions then move to a $110°$ analysing magnet, which bends the ions into the beamline for further transportation. This magnet allows for selection of mass and charge state of the ion, since the deflection of the ion by the magnetic field depends on the ratio of mass to charge. A Faraday cup is placed after the analysing magnet, which allows for measurements of the ion current for a given magnet strength. Since the magnet selects on mass over charge, it is possible for the desired ion beam to be contaminated with undesired ions with the same mass over charge ratio. Therefore, isotopes are selected with a unique mass over charge ratio compared to other elements present in the ion source. By sweeping over the magnet strength and measuring the ion beam current, individual isotopes and charge states can be identified. This also allows for identification of the particles that are present in the ion source. At a set magnetic field strength of the magnet, ions bent correctly into the beamline will be transported further. Other ions will collide with the wall of the beamline. From the current measurement of the ion beam by means of the Faraday cup, the beam current is optimized by adjustment of RF source power, bending magnet strength, pressure in the ion source and puller electrode and lens settings. Additionally, it is possible to add a second gas to the ion source such as helium, which can potentially stabilize the plasma and change the ion distributions in the ion source.

3.2 Transportation of ion beam

After optimization of the beam current, the beam is transport to the CHEOPS setup. Transportation is facilitated by two triplet quadruple focusing magnets and two correction magnets. The triplet quadruple magnets focus the ion beam, such that the transmission is improved. They consist of three instances of quadrople magnets. The first and last of the magnets focus in one direction, while the middle magnets focus in the plane perpendicular to this direction. The two correction magnets are placed some distance apart and allow for a correction of the trajectory of the ion beam. The correction magnets can bend the ion beam slightly in the vertical and horizontal direction. The correction magnets correct for deviations of height and horizontal direction of the ion beam, as well as for deviations in alignment of the beamline. After the ion beam has passed the second triplet quadruple magnet, it arrives at a $45°$ bending magnet. This magnet is used to bend the ion beam towards CHEOPS.

3.3 CHEOPS

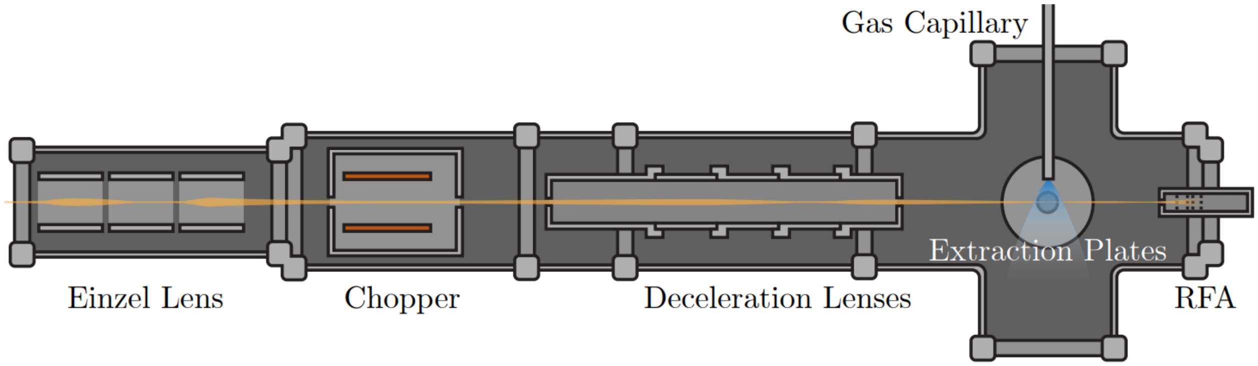

Figure 3.2: Schematic of an ion beam travelling through CHEOPS. The ion beam can be focused by the Einzel lens and the deceleration lenses. Gas can be injected into the chamber by the gas capillary. The ion beam current is measured by the retarding field analyser (RFA). The chopper can be used to send a pulsed ion beam into the chamber.

At CHEOPS, ion-hydrogen interactions take place. A schematic of this setup can be seen in figure 3.2. The ion beam first passes an einzel lens, which is used to focus the ion beam once again. Then it passes a chopper, which allows for pulsing of the ion beam. For the measurements done in this thesis, the chopper is not used. The ions then pass the deceleration lenses. These lenses create a potential which can decelerate and focus the beam. The final deceleration of the ion beam depends on the potential present after the deceleration lenses, which is described in the next subsection. After passing the deceleration lenses, the ion beam enters the collision chamber. In the collision chamber, a gas capillary is present, which injects a jet of hydrogen gas into the chamber. The position of the capillary can be adjusted, which can be used to change the density of gas particles the ion beam encounters. The rate of hydrogen gas entering the chamber is determined from the pressure in the foreline of the capillary. In turn, this pressure is regulated by a mass flow controller (MFC), which allows for precise control of the rate of hydrogen flowing into the chamber. When the ion beam reaches the chamber, collisions with hydrogen take place and charge transfer can occur. After these collisions, the ion beam is not uniformly charged anymore, but consists of ions of different charge states.

After collisions with hydrogen, the ions enter the retarding field analyser (RFA). The retarding field analyser consists of multiple cylindrical electrodes. In figure 3.3, a schematic of the RFA can be seen. The first grounded electrode shields the collision chamber from the electric field of the retarding electrode. The retarding electrode imposes an electric field on the ions, creating a potential barrier that ions can only pass if they possess sufficient kinetic energy. Another grounded electrode is located on the other side of the retarding electrode. This electrode shields the potential of the retarding electrode, such that the suppressing electrode is not influenced by the field of the retarding electrode. The suppressing electrode creates an electric field which repels any outgoing electrons from the Faraday cup. These secondary electrons can be created when the ions collide with the Faraday cup. When an electron leaves the Faraday cup, it is measured as a current. The suppressing electrode causes electrons to move back into the Faraday cup, such that no net current of emitted electrons is measured.

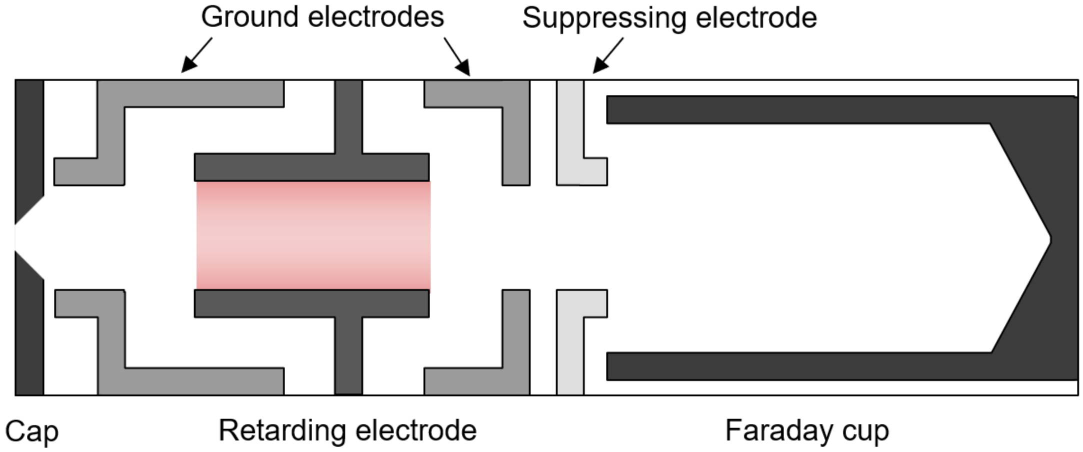

Figure 3.3: Cross section of a gridless RFA. The retarding electrode creates a potential barrier for incoming ions. The grounding electrodes shield the collision chamber and suppressing electrode from the electric field of the retarding electrode. The suppressing electrode prevents electrons from leaving the cup.

The retarding electrode is significantly longer than the other electrodes. It was designed in this way, such that the radial potential at the retarding electrode is more uniform compared to shorter electrodes. When a voltage is placed on the retarding electrode, the potential near the electrode itself will be higher than the potential at the centre of the electrode. This potential difference may cause ions with the same kinetic energy, to either be transmitted to the Faraday cup or be repelled, depending on which region of the RFA they pass through. The ratio between the potential at the retarding electrode and the centre of the electrode is characterised by the k value of the electrode. According to simulations performed for this system, the k value is approximately 0.99 [11]. When ions are transmitted through the electrode, they are collected in the cup, which creates a measurable current. By placing a voltage on the retarding electrode, ions can be repelled. The voltage at which this occurs depends on the kinetic energy and the charge state of the incident ions. The ions are repelled when the following condition is satisfied:

$$qV_r > E_{kin} \tag{3.3}$$

Where E_{kin} is the kinetic energy of the ions in eV. When this condition is satisfied for ions of charge q, it will be seen as a drop in the current measured at the Faraday cup. By variation of the retarding voltage and measurement of the corresponding current, the amount of ions of charge state q can be found. From these measurements, charge transfer cross sections can be determined. A voltage sweep of the RFA can be seen in figure 3.4 where a decelerated 8 keV Sn^{4+} ion beam was used. In this figure, the current drops significantly at certain voltages. The current drops correspond to the RFA stopping ions of a certain charge state from reaching the Faraday cup. Additionally, two contamination currents *Sn^{3+} and *Sn^{2+} are shown in figure 3.4, which correspond to ions that have undergone charge transfer before being decelerated. These contamination currents can be filtered out and are a byproduct of deceleration of the ion beam.

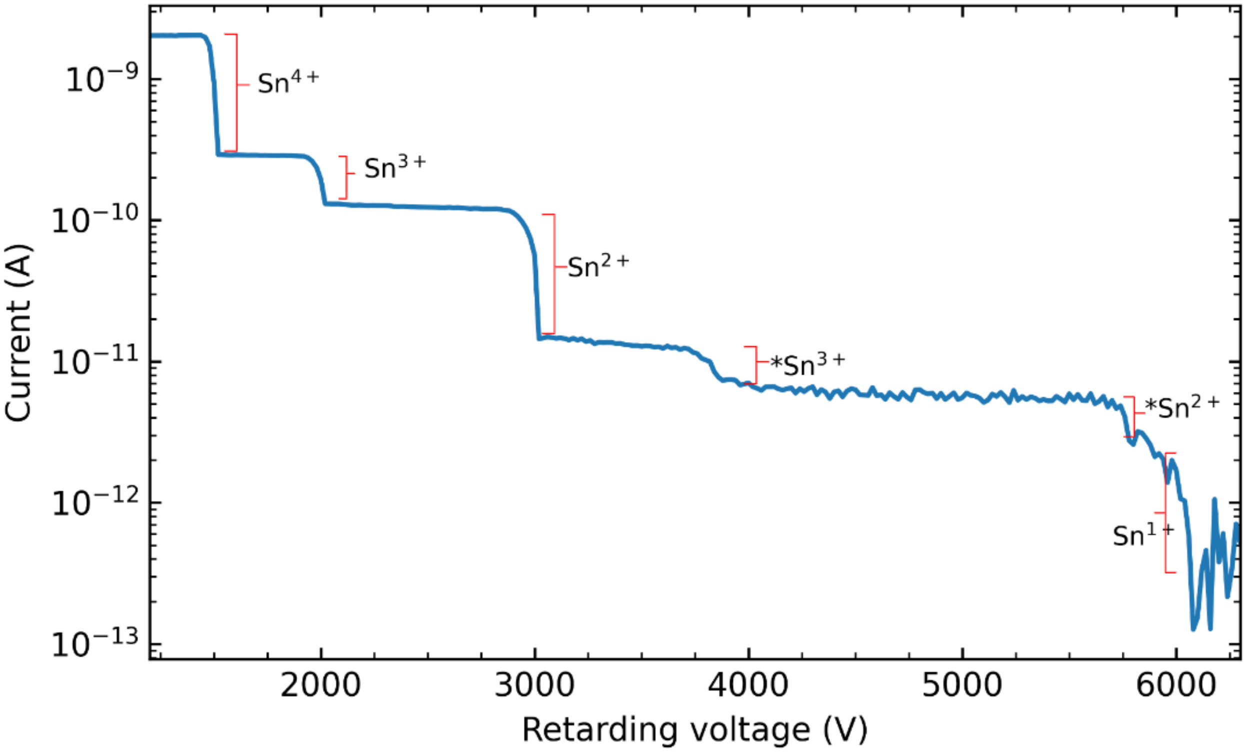

Figure 3.4: Voltage sweep of the RFA for a decelerated 6 keV Sn^{4+} ion beam after collisions with hydrogen. The drop in current can be attributed to the stopping of different ions at certain voltages. Contamination currents are marked by an asterisk.

3.4 Deceleration of the ion beam

The kinetic energy of the ions arriving at CHEOPS is determined from their charge state and the voltage on the source. By decelerating the beam before it enters the collisions chamber, it is also possible to change the kinetic energy of the ions. This procedure has two main benefits. It allows for measurement at different kinetic energies without requiring adjustment of the settings used for transportation of the beam. Additionally, decelerating the ions after transportation is preferred, since transmission of the ion beam is improved at higher kinetic energies. In order to decelerate the ions, the entire CHEOPS setup is put on a voltage which is equal to the voltage of the ion source. Ions arriving at CHEOPS see a potential barrier which decelerates them. A voltage supply is used to lower the voltage of CHEOPS by an amount of V_{bias}. The kinetic energy of the ions at CHEOPS then becomes:

$$E_{kin} = q(V_{bias} + V_{plasma}) \tag{3.4}$$

Because of the potential barrier caused by the voltage on CHEOPS, the ion beam will diverge and the amount of ions entering the collision chamber will be lower initially. Four deceleration lenses are used to correct for this which reduce the potential before ions enter the collision chamber. This allows for a more gradual potential gradient and focuses the ion beam. Deceleration of the ion beam also introduces the contamination currents described earlier. Since these ions have had charge transfer before they are decelerated, they are decelerated less at the deceleration stage compared to the higher charged ions. The kinetic energy of these contamination ions when they arrive in the collision chamber is:

$$E_{kin} = qV_{bias} + V_{plasma} + n_c(V_{source} - V_{bias}) \tag{3.5}$$

where n_c is the number of electrons that are captured before deceleration. The contamination current can be filtered out by measuring the current at a voltage before and after the contamination current is stopped. An additional benefit of a decelerated beam is that charge transfer processes which do not occur inside the reaction chamber can be filtered out this way. Measurements are then independent of residual gas present in other parts of the system.

4 Characterisation of experimental setup

Before cross section measurements were started, characterisation measurements of the gridless RFA and the tin oven were performed. In previous charge transfer cross section measurements, ion currents were measured using a gridded RFA. For measurements performed in this thesis, a gridless RFA was used. Before cross sections measurements could be performed, characterisation of the gridless RFA was necessary in order to account for any unforeseen effects. Additionally, characterisation measurements of the tin oven were performed. During charge transfer cross section measurements, a stable ion beam current is desirable to improve the accuracy of the measurements. Therefore, measurements were performed to analyse if improvements to the reliability of the tin oven could be made. The results of these characterisation measurements are laid out in this section.

4.1 Characterisation of gridless RFA

The gridless RFA was implemented to increase transmission and reduce lensing effects over the gridded RFA. After implementation of the gridless RFA, transmission was improved, but some unaccounted for effects were still present. Additional measurements were performed to characterize these effects. Figure 4.1 shows voltage sweeps of a Xe^{4+} beam, with different voltages placed on the third deceleration lens. The voltage placed on this lens changes the focus of the ion beam. In the figure, three regions of interest can be seen. First, it can be seen that the current starts to drop at voltages much lower than the voltage required to repel the ions, as determined from equation 3.3. Then, a small peak can be seen at 5025V, after which there is a final region where the current drops of rapidly towards zero. This final region can be attributed to the fact that ions passing through different regions of the RFA experience a slightly different potential, causing some ions to be repelled and others to still be transmitted. This can explain the effect that the current does not drop off instantly in this region. Instead, it drops off with a slope, which is as expected. The effects in the other regions appear to depend on the focus of the ion beam.

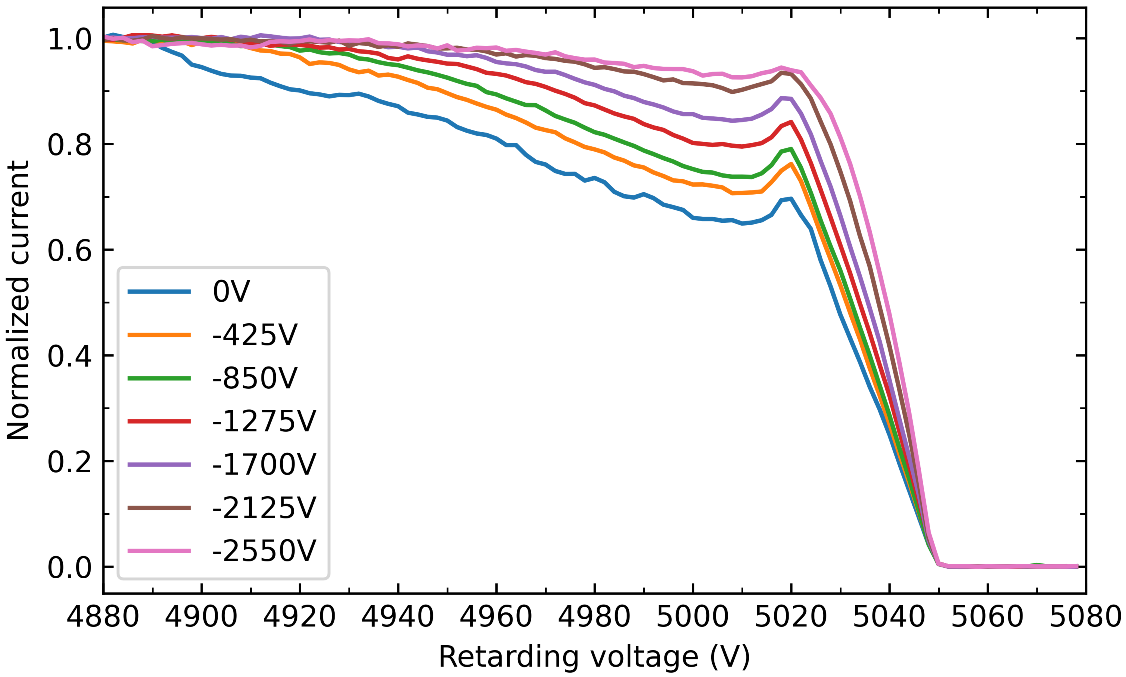

Figure 4.1: Voltage sweeps of a 20 keV Xe^{4+} beam with different voltages placed on deceleration lens 3, which changes the focus of the ion beam. The graph shows that changing the focus of the ion beam can mitigate the observed effects present in the RFA.

Other measurements were performed by moving the position of the RFA and taking voltage sweeps. The position of the RFA can be moved in two orthogonal directions, denoted by the x direction in the horizontal plane and the y direction in the vertical plane, orthogonal to the direction of the ion beam. The results can be seen in figure 4.2, where voltage sweeps were taken with a 28 keV Ar$^{4}+$ beam. The measurements were performed without a voltage on deceleration lens 3, denoted by an ”unfocused” ion beam and then repeated with a voltage on the deceleration lens, denoted by ”focused”. The RFA was first centered by noting the position in x and y direction at which the measured current was zero. For each direction, the centre was taken as the centre between each distance. The position of the RFA was then changed relative to this position. For a homogeneous beam which enters the RFA at no angle, it is expected that the voltage sweeps show symmetry when displaced by the same amount in opposite directions. However, it can be seen in figure 4.2 that this is not the case. While the voltage sweeps for displacement in the x direction still show some symmetry, the sweeps for the y direction are much more asymmetric. A reason for this could be that the RFA is placed at an angle in the beamline, or that the ion beam itself enters the RFA under an angle. When this happens, the ion beam passes through different potential regions of the RFA. It is also possible for the ion beam to simply hit the electrodes of the RFA. From figure 4.2, it seems that the angle at which the beam enters the RFA is located in the y direction plane, since the asymmetry is much more present there. From the characterisation of the RFA it is seen that the current starts to decrease before the final retarding voltage is reached. During cross sections measurements, energies can be selected in such a way that ion populations are not stopped close to each other. This allows for measurements at voltages which are significantly far away from the stopping voltages. At these voltages, the observed effects are not present. Therefore, there should be no influence by these effects on the measurement of the ion populations. Further analysis of the behaviour of the gridless RFA was performed by [12].

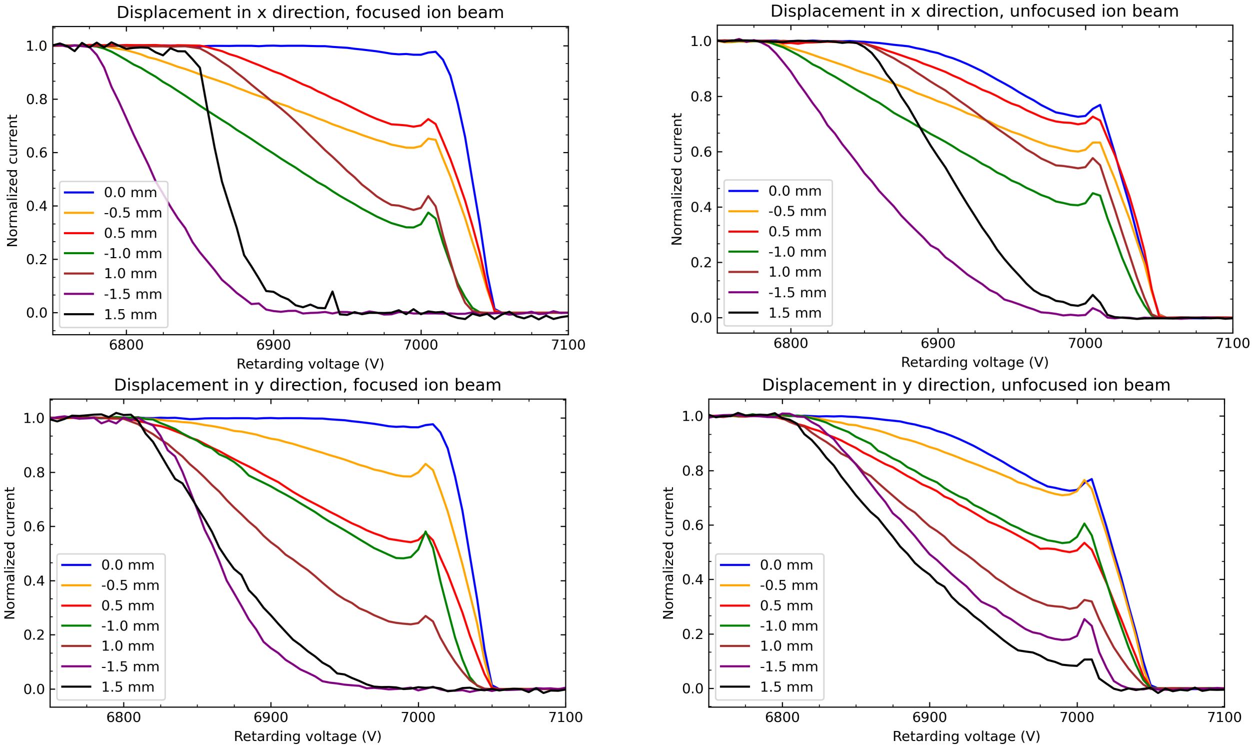

Figure 4.2: Voltage sweeps performed for different displacements of the RFA from the centre of the ion beam. Displacement were done in two different direction, x and y. For each displacement, a voltage sweep was taken for an unfocused beam and for a focused beam. It is seen that asymmetry is more present in the y direction, suggesting that the ion beam enters the RFA under an angle in this direction.

4.2 Characterisation of tin oven

In this subsection, the main results from the characterisation of the tin oven are presented. The goal of the experiment was to characterise the tin oven in such a way, that its behaviour is understood better and possible improvements could be implemented. The experiment was performed by evaporating tin from the tin oven on a quartz crystal, which is able to measure the thickness of the evaporated tin layer on the quartz by change in the eigenfrequency of the quartz crystal. From the change in thickness of the tin layer, the rate of tin evaporating on the quartz is measured. Most importantly, the relation between power input and evaporation rate was investigated as well as the mechanisms of energy loss for the tin oven.

The experimental setup consists of a tin oven and a quartz crystal placed in a vacuum chamber. By applying a voltage to the tin oven, a current runs through the tungsten filaments around the oven, heating it up such that tin evaporates and leaves the oven. Some of the evaporated tin that leaves the oven will be deposited on the water cooled quartz crystal opposite of the oven. The quartz crystal has a specific frequency that changes when a material is

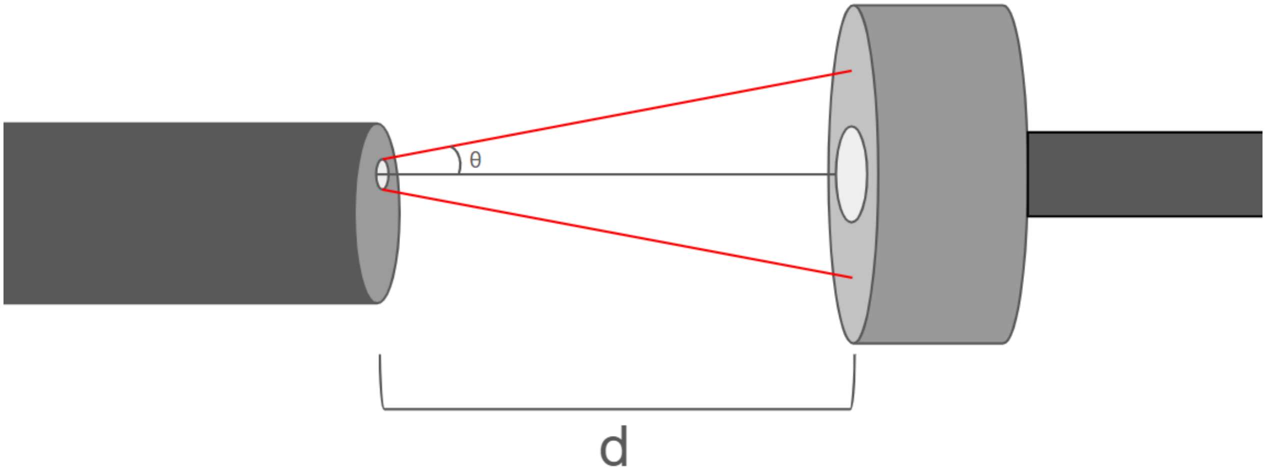

Figure 4.3: Experimental setup of the characterisation measurement of the tin oven. A quartz crystal was placed some distance d away from the tin oven. When the tin oven is heated, tin evaporates and is deposited on the quartz crystal. From the change of the eigenfrequency of the quartz crystal, the deposition rate of tin on the crystal is determined.

deposited on top of it, allowing for a determination of the thickness of the deposited layer. The setup can be seen in figure 4.3. In this figure, the tin leaves the oven at a maximum angle θ and the crystal is placed at a distance d from the oven. The source of the tin can be seen as a point source located inside the tin oven, adding an offset to the actual distance from the point source to the quartz crystal. By measuring the deposition rate of tin on the quartz crystal, the influence of input power fluctuations on rate fluctuations can be found.

In figure 4.4, the deposition rate of the tin on the quartz crystal and the power input of the tin oven are plotted. During this measurement, a constant voltage was placed on the tungsten filament in the tin oven. However, as can be seen, the power fluctuates constantly. Around 10.000 seconds, a sudden drop in power is seen and a corresponding drop in deposition rate as well. After some time, the power suddenly increases again. What causes this sudden change in power remains unknown. Smaller fluctuations in the power input can be attributed to changes in the resistance of the tungsten filament, due to heating. From figure 4.4, it is clear that the deposition rate fluctuations are influenced by fluctuations in the power. By controlling the tin oven by a constant power input instead of a constant voltage input, these fluctuations can be eliminated. This constant power control was subsequently implemented and used during charge transfer cross section measurements.

Additionally, the energy loss of the tin oven can be examined. By determination of the ratio of energy loss by latent heat due to evaporation of tin and black body radiation radiated by the tin oven, an estimation can be made whether evaporation of tin has a significant effect on the temperature of the oven. The energy loss from black body radiation can be found from:

$$P_{bb} = \epsilon \sigma A T^4 \tag{4.1}$$

where ϵ is the emissivity of the tantalum casing of the tin oven, which is approximately 0.33 for tantalum [13], A is the surface area of the casing and T is the temperature of the casing. The

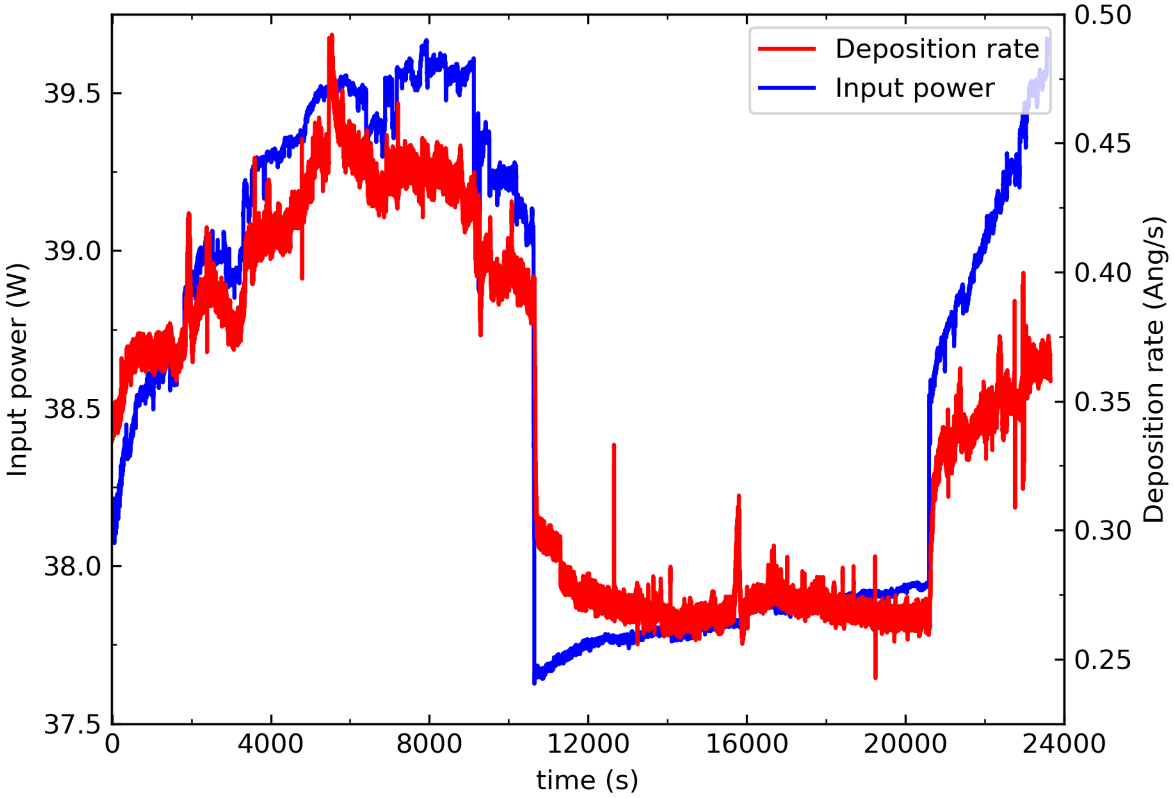

Figure 4.4: Rate of tin deposited on the quartz crystal as well as power input on the tin oven. It can be seen that tin output from tin oven is influenced by fluctuations in the power input.

temperature of the casing can be determined by measuring the temperature with a pyrometer. The energy loss from tin evaporation can be determined from the amount of tin leaving the oven per second η multiplied by the latent heat:

$$P_{evaporation} = L \cdot \eta \tag{4.2}$$

where L is the latent heat, which has a value of 295.8 kJ/mol. A rough estimation of the amount of tin leaving the oven per second can be made after measurement of the weight of the tin oven before and after the tin inside has been evaporated. From these equations, it was found that the energy loss from evaporation of tin is about 5 order of magnitude smaller than the energy loss from black body radiation. As a conclusion, the temperature of the tin oven is independent of the amount of tin present in the oven.

5 Methods

During collisions of Sn^{4+} with H$_2$, charge transfer occurs via different processes. After a collision with H_2 the initial Sn^{4+} ion can become a Sn^{3+} ion or a Sn^{2+} ion, depending on which charge transfer process has taken place. Additionally, secondary collisions can occur. If this is the case, an ion that has already undergone charge transfer, will undergo charge transfer again. Therefore, there are multiple pathways for an Sn^{4+} ion to become an Sn^{2+} or a Sn^{1+} ion. The entire chain of charge transfer processes can be described by an initial value problem, where the ions move through a volume of hydrogen gas density described by $n(z)$:

$$\begin{bmatrix} \frac{dN^{4+}}{dz} \\ \frac{dN^{3+}}{dz} \\ \frac{dN^{2+}}{dz} \\ \frac{dN^{1+}}{dz} \end{bmatrix} = n(z) \begin{bmatrix} -\sigma_{43}-\sigma_{42} & 0 & 0 & 0 \\ \sigma_{43} & -\sigma_{32}-\sigma_{31} & 0 & 0 \\ \sigma_{42} & \sigma_{32} & -\sigma_{21} & 0 \\ 0 & \sigma_{31} & \sigma_{21} & 0 \end{bmatrix} \begin{bmatrix} N^{4+} \\ N^{3+} \\ N^{2+} \\ N^{1+} \end{bmatrix}, \quad N(z=0) = \begin{bmatrix} N_0 \\ 0 \\ 0 \\ 0 \end{bmatrix} \tag{5.1}$$

where σ_{ij} is the charge transfer cross section for an ion of charge i to become an ion of charge j and N^i the amount of ions in charge state i. It is assumed that the total number of ions is conserved, such that:

$$N_0 = N^{4+} + N^{3+} + N^{2+} + N^{1+} \tag{5.2}$$

The integral of $n(z)$ is defined as the integral target density described by:

$$\int n(z)dz = \beta P \tag{5.3}$$

where β is a calibration constant. From previously performed density calibration measurements, such as in [14], β was determined to be $65 \pm 4 \cdot 10^{16}$ cm^{-2} mbar^{-1}.

5.1 The single collision approximation

The solution to equation 5.1, is rather complicated and cumbersome to work with, therefore the process is initially regarded in the single collision approximation. In other words, an ion will only undergo only one charge transfer process. In this approximation only σ_{43} and σ_{42} will be non-zero in equation 5.1. All other cross section will be zero. The solutions to equation 5.1 then become:

$$N^{4+} = N_0 e^{-\beta P(\sigma_{43}+\sigma_{42})} \tag{5.4}$$

$$N^{3+} = N_0 \frac{\sigma_{43}}{\sigma_{43}+\sigma_{42}}[1 - e^{-\beta P(\sigma_{43}+\sigma_{42})}] \tag{5.5}$$

$$N^{2+} = N_0 \frac{\sigma_{42}}{\sigma_{43}+\sigma_{42}}[1 - e^{-\beta P(\sigma_{43}+\sigma_{42})}] \tag{5.6}$$

From these equations, the ratio between N^{2+} and N^{3+} can be expressed as a constant f:

$$\frac{N^{2+}}{N^{3+}} = \frac{\sigma_{42}}{\sigma_{43}} = f \tag{5.7}$$

From this ratio, σ_{43} and σ_{42} can be determined directly from the equations:

$$\sigma_{43} = -\frac{\ln \frac{N^{4+}}{N_0}}{(1+f)\beta P} \tag{5.8}$$

$$\sigma_{42} = f\sigma_{43} \tag{5.9}$$

Since measurements are done at pressures up to 10^{-4} mbar, this approximation will be fairly accurate. In order to account for secondary collisions to some degree, it is possible to determine the cross sections at different pressures. Through a linear fit through these cross sections, an extrapolation of the cross section to zero pressure can be done. This allows us to correct for secondary collisions.

5.2 Determination of charge transfer cross sections

After collisions of the tin ions with the hydrogen molecules, ion populations are determined from measurements with the RFA. These measurements are performed in cycles, where the RFA cycles through retarding voltages. The retarding voltages are set specifically to measure the ion populations and to filter out contamination current if present. Multiple cycles are used to improve the significance of the data. In figure 5.1, an example of such a measurement can be seen. In this figure, the retarding voltage is changed and the corresponding decrease in ion current corresponds to different ions of different charge states and contamination current. During measurements, it is important for the ion beam current to constant. Measured ion populations are normalised by the total amount of ions measured in each cycle. When the current changes during a cycle, the affected measured ion populations will change as well, affecting the results. Ion beam current changes can happen due to a multitude of reasons, such as heating of transportation magnets, plasma instabilities or tin oven output. When significant changes in ion beam current occur, the corresponding measurements are taken out of the data set.

Initially, cross section measurements were performed with a ^{120}Sn^{4+} beam, since this tin isotope is the most abundant. After some measurements were performed, it was noticed a contamination ion with the same mass over charge ratio was present in the ion beam. Because of the contamination, measurements were repeated for ^{118}Sn^{4+}, which is the second most abundant isotope of tin. For the measurements, a 28 keV ^{118}Sn^{4+} ion beam was used and decelerated to a range of different energies from 1 keV up to 16 keV. For each energy, measurements were performed at three different pressures of approximately $16.9 \cdot 10^{-5}$, $8.4 \cdot 10^{-5}$ and $4.3 \cdot 10^{-5}$ mbar. In figure 5.2, cross sections calculated for different pressures using equations 5.8 and 5.9 are shown. A linear fit was performed to extrapolate the cross sections to zero pressure. The final cross sections σ_{43} and σ_{42} are then determined as the value of the linear fit at zero pressure.

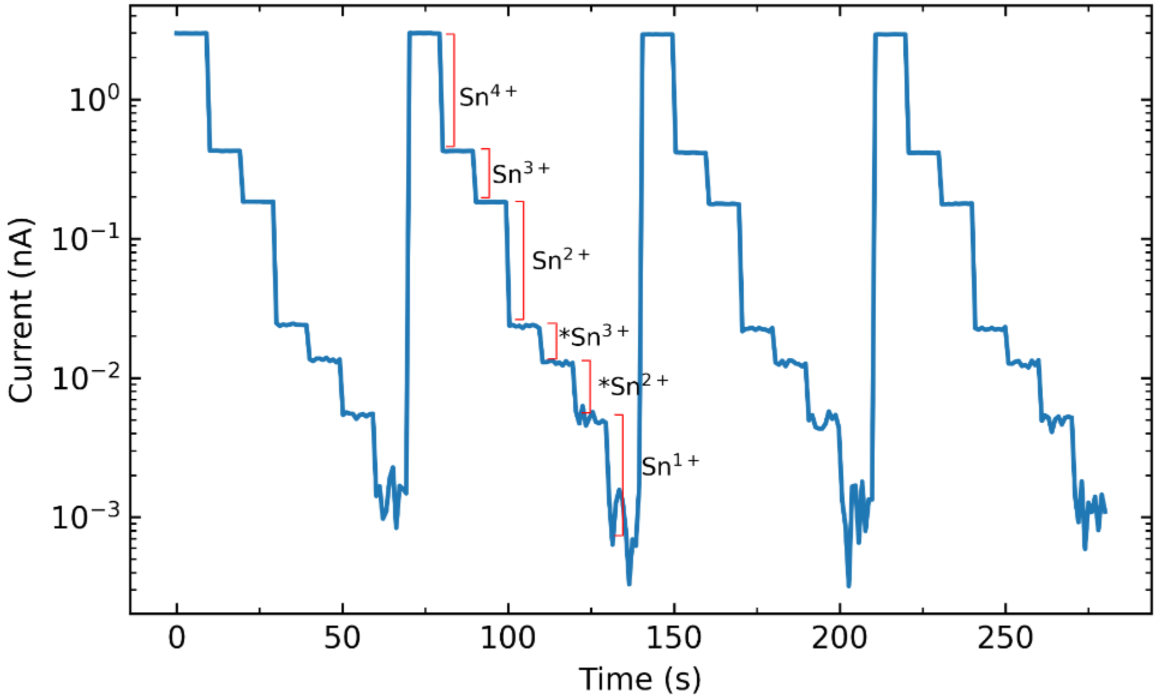

Figure 5.1: Measurement of ion current at different voltages for an 8 keV ion beam. From these measurements the ion populations are determined from which cross sections are calculated. Measurements are performed in cycles seen in the image, which are used to determine the error in the measurements.

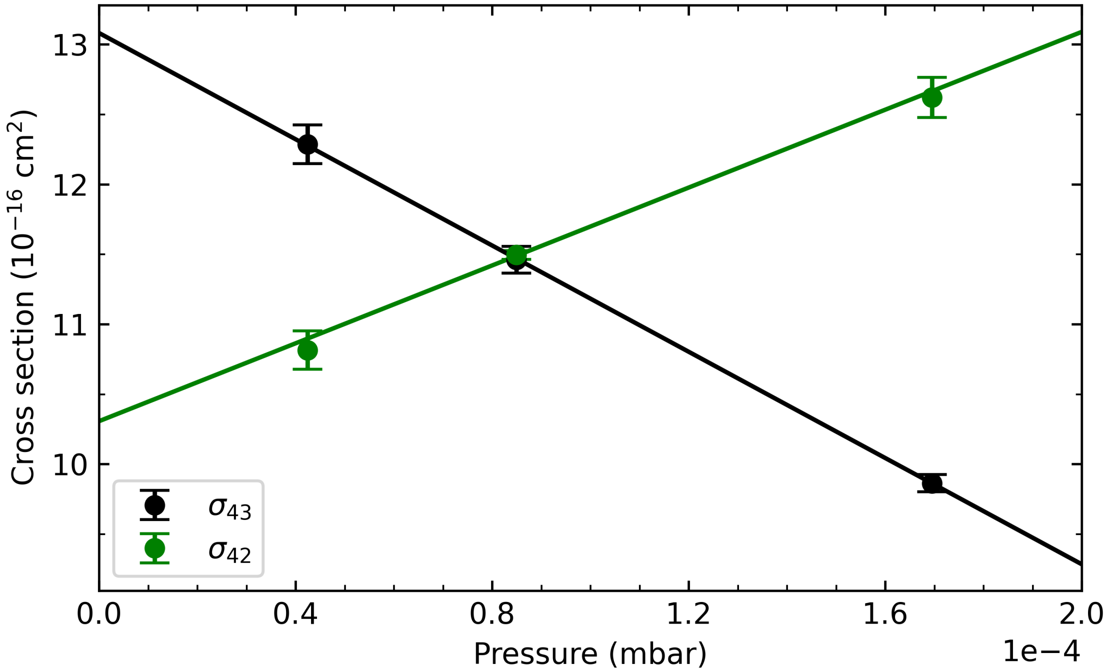

Figure 5.2: Figure showing extrapolation of the calculated cross section at different pressures for a 2 keV ion beam. By extrapolating to zero pressure, a correction is made for secondary collisions.

6 Contamination of the ^{120}Sn^{4+} ion beam

Initial measurements of cross sections performed with a ^{120}Sn^{4+} beam were found to be contaminated with some unknown contamination ion. In this section, the ion is identified and it is investigated whether the measurements still have some value. In figure 6.1, two magnet scans can be seen. The left image shows a magnet scan with a large tin current, where the isotopes are clearly distinguishable. The right image shows a magnet scan where no tin was injected into the ion source. In this image, a peak at mass over charge 30 is clearly visible, indicating a contamination ion.

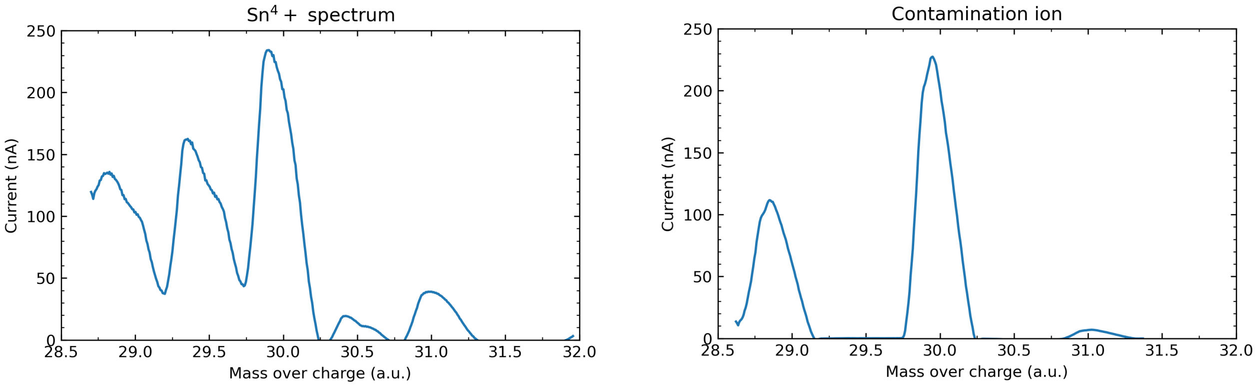

Figure 6.1: Magnet strength sweep performed when tin is present in the ion source (left) and when no tin was present and ion source was recently exposed to air (right).

In figure 6.2 a magnet scan can be seen over a large range of mass over charge. This magnet scan was taken after the ion source had recently been exposed to air. Therefore, large amounts of ion current are present due to elements present in the air. In the figure, several ions have been identified of which most are gases that are present in air. Other possible ions that are considered to be present in the plasma chamber are metals which can come from the components that are present in the plasma chamber and noble gases which have previously been used for measurements. Elements can be identified through their mass over charge ratio, as well as the presence of isotopes of these elements in the correct ratios. From the magnet scan, it was found that metal ions are not present in the plasma chamber in any significant amounts. Additionally, the noble gases that were used in the plasma chamber do not have any isotopes with a mass over charge ratio of 30. Only one gas in the atmosphere has a mass over charge ratio of 30, which is ^{15}N$_2^{1+}$. However, the ^{15}N isotope has an abundance of only 0.4%. If the contamination would be present due to ^{15}N$_2^{1+}$, currents at a mass over charge ratio of 29 and 28 should have been much higher. One other possible ion could be Si^{1+}, which has three stable isotopes of mass 28, 29 and 30. Silicon is used for lubricants present in the ion beam system. However, the natural abundance of Si isotopes should result in a higher current peak at mass over charge 29 compared to 30, which is not the case. Additionally, the current at 29 mass over charge also has the current contribution from N$_2^{1+}$ where the molecule has one ^{15}N and one ^{14}N isotope. Therefore, it is more likely for the contamination ion to be an ion that is formed inside the plasma chamber itself. From the magnet scan, it can be seen that many molecules have dissolved into their respective elements, such as H$^+$, C$^+$, N$^+$ and O$^+$ from H_2O, O_2 N_2, and CO_2. It is possible for these elements to react into other molecules inside the ion source. Therefore, it is likely that the contamination ion is a nitric oxide ion (NO^+), which is formed in the ion source from nitrogen and oxygen ions. Formation of NO^+ in the presence of N_2 and O_2 in plasma conditions has also been observed by other authors [15]. Additionally, an ion beam consisting solely of the contamination ion was transported and a voltage sweep was performed after the ion beam had collided with hydrogen in the collision chamber. In this measurement, current dropped off in a single step. This indicates that the contamination ion either does not experience any charge transfer or that it has a charge of 1. Analysis of particle conservation of charge transfer measurements with the $^{120}Sn^{4+}$ ion beam show that the amount of particles are generally conserved. This indicates that the contamination ion does not experience any charge transfer.

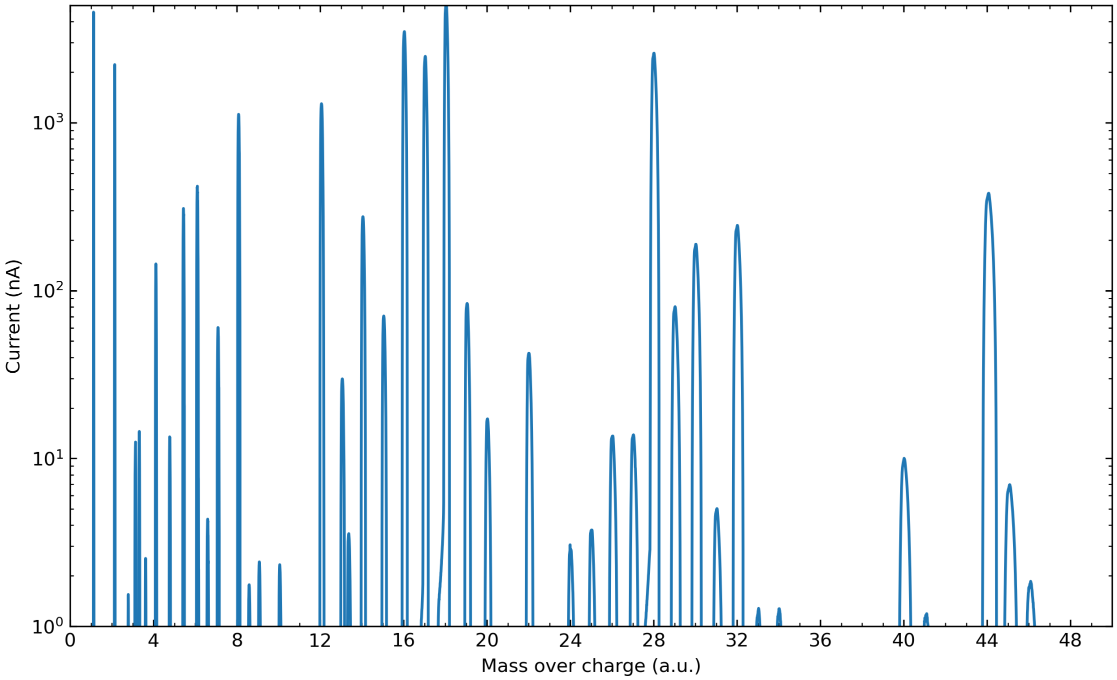

Figure 6.2: Magnet strength sweep after the ion source was recently exposed to atmosphere. High currents can be seen at mass over charge corresponding to elements present in air.

Due to the presence of the contamination ion, the Sn^{4+} ion population will become artificially higher than it is in reality. Additionally, the total amount of ions, N_0, is inflated as well. The amount of contamination ions present in the ion beam will depend on many factors such as the amount of RF power sent into the ion source and the time since the ion source was last exposed to atmosphere. Therefore, the contamination current is not constant and cannot be filtered out of the data. To conclude, results of the $^{120}Sn^{4+}$ measurements cannot be used for determination of the charge transfer cross section due to the contamination.

7 Measurements of collisions of Sn^{4+} with H$_2$

In figure 7.1, the determined cross sections for single electron capture σ_{43} and for double electron capture σ_{42} are plotted for different kinetic energies of the projectile. Additionally, charge transfer cross sections from measurement of Sn^{3+} determined in [16] are plotted. The first experimental data point shows the systematical error caused by the error in the calibration constant β. This error will cause all experimental values to shift up or down equally. It can be seen that experimental values for σ_{43} have a plateau at energies of 1.5-8 keV and appear to increase at higher energies. The experimental values for σ_{42} appear to peak around 3 keV and seem to decrease at lower and at higher energies. The decrease of the cross section for double capture is much weaker than for Sn^{3+}. The fact that the double capture cross sections decrease at higher energies could suggest that a longer interaction time is required for double electron capture to effectively take place.

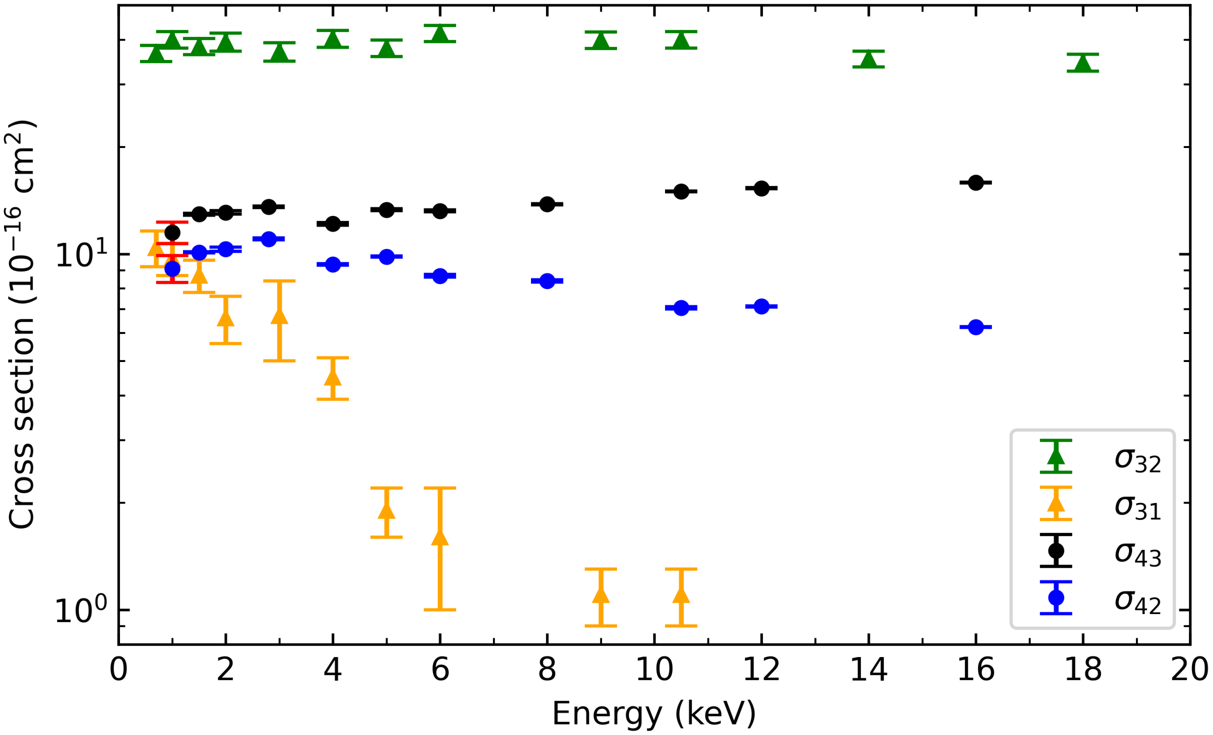

Figure 7.1: Experimentally determined charge transfer cross sections for Sn^{4+}-H$_2$ collisions. Experimental values for Sn^{3+}-H$_2$ collisions, σ_{32} and σ_{31} are added for comparison, adapted from [16]. The red error bar indicates the overall systematical error due to the uncertainty in the calibration constant β.

The experimental values found for σ_{43} are about 3 times smaller than the values for σ_{32}. From classical theory, it is expected that for a higher charged state, a larger charge transfer cross section is expected, as can be seen from equations 2.10 and 2.11. The reason for the fact that σ_{43} is smaller than σ_{32} can understood via a combination of the overbarrier model and potential energy curve crossings. In figure 7.2, curve crossings can be seen of Sn^{4+} +

H_2 with Sn^{3+} + H_2^+ and of Sn^{3+} + H_2 with Sn^{2+} + H_2^+. The radius for electron capture R_c calculated from equation 2.9 is indicated in each figure. For single capture from Sn^{3+} into Sn^{2+}, three states are immediately present at this radius. For single capture from Sn^{4+} into Sn^{3+} it is seen that the first state where charge transfer can occur is at a radius much smaller than R_c. The effective cross section for electron capture is therefore understood to be much smaller for Sn^{4+} compared to Sn^{3+}. A crude estimation can be made by comparing the ratio of the curve crossing distances squared between the two different systems. This ratio is about 0.5, which suggests that the cross section for Sn^{4+} should be 2 times smaller as compared to Sn^{3+}. In the experimental results, this cross section is about 3 times smaller. However, the double electron capture cross section needs to be considered for Sn^{4+} too. Double and single electron capture can be seen as competitive processes, since single electron capture cannot occur when double electron capture occurs. Therefore, it is possible for the single electron capture cross section for Sn^{4+} to be even smaller due to competition with double electron capture, which consumes part of the overall cross section. For collisions of Sn^{3+} with hydrogen this competition is barely present, since double electron capture cross section is very unlikely.

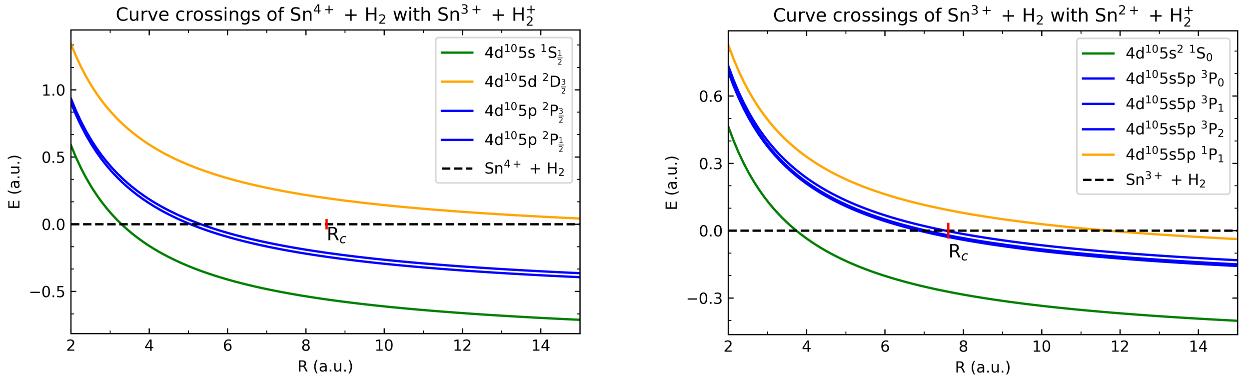

Figure 7.2: Curve crossings for Sn^{q+} + H_2 with $Sn^{(q-1)+}$ + H_2^+ for initial Sn^{4+} and Sn^{3+} ions. The radius for electron capture calculated from the over barrier model is indicated in each graph by R_c. While the electron capture radius from the overbarrier model for Sn^{4+} is larger compared to Sn^{3+}, the only state where the electron can be captured into is at a much smaller radius.

In figure 7.3, σ_{43} is plotted as well as multichannel Landau-Zener calculations of σ_{43} for different initial states of the Sn^{4+} ion. The Landau-Zener calculations for electron capture from the Sn^{4+} ground state of $4d^{10}\ ^1S_0$ are roughly 30% lower than the experimental values, but show a similar evolution. For kinetic energies lower than 5 keV, the calculations deviate much more from experimental results. Such behaviour has also been found by other authors [8]. The Landau-Zener calculations from ground state Sn^{4+} were performed for transitions into the Sn^{3+} states $4d^{10}5p\ ^2P_{\frac{1}{2}}$ and $^2P_{\frac{3}{2}}$. It was found that transitions from the ground state of Sn^{4+} into other Sn^{3+} states have a negligible contribution to the cross section, as calculated by the Landau-Zener model. Additionally, Landau-Zener calculations were performed for electron capture from multiple excited Sn^{4+} states to assess a possible role of metastable Sn^{4+} ions. The lifetimes of the excited Sn^{4+} $4d^95s\ ^3D_2$, $^3D_1$ and $4d^95s\ ^1D_2$ states have been estimated by some to be 171 μs, 1430 s and 42 μs respectively [17]. The amount of time it takes for the ions to move from the ion source to CHEOPS is in the order of 60 μs for the 28 keV ion beam that was used. The lifetimes of the excited state ions are long enough for the ions to reach CHEOPS in an excited state. The lifetime for the Sn^{4+} 4d^{9}5s ^{3}D$_3$ state was not calculated by the authors. However, it can be speculated that this ion would also have a similar lifetime. It is reasonable to assume that if metastable excited Sn^{4+} ions are produced by the ion source, they live long enough to undergo collisions in the setup. Consequently, the presence of these states influence the cross sections that were measured. The Landau-Zener calculations for the 4d^{9}5s ^{3}D$_3$, ^{3}D$_2$ and ^{3}D$_1$ levels of Sn^{4+} were performed for electron capture into the 4d^{9}5s(^{3}D)5p ^{2}P$_{\frac{1}{2}}$, 4d^{9}5s(^{3}D)5p ^{2}P$_{\frac{3}{2}}$, 4d^{9}5s(^{3}D)5p ^{4}D$_{\frac{1}{2}}$, 4d^{9}5s(^{3}D)5p ^{4}P$_{\frac{1}{2}}$ and 4d^{9}5s(^{3}D)5p ^{4}P$_{\frac{3}{2}}$ levels of Sn^{3+}. For the Landau-Zener calculations, energies were used as determined in [18] and [19]. These levels were specifically chosen for the similar core structure of 4d^{9}5s(^{3}D) of the initial and final state as well as adherence to spin conservation of the initial and final state after electron capture. As can be seen in figure 7.3, the Landau-Zener calculations for initial states 4d^{9}5s ^{3}D$_3$ and 4d^{9}5s ^{3}D$_2$ are of similar magnitude as the experimental results for energies of 4 keV or higher. The Landau-Zener calculation for the initial state 4d^{9}5s ^{3}D$_1$ are almost equal to the cross section calculated for the ground state of 4d^{10} ^{1}S$_0$ of Sn^{4+}. The Landau-Zener calculation for the initial state 4d^{9}5s ^{1}D$_2$ displays significant deviation from the experimental values. If the different initial Sn^{4+} states are present in the ion beam, each state will have its own contribution to the measured cross section, multiplied by its abundance in the ion beam. Since the lifetime of the 4d^{9}5s ^{1}D$_2$ is estimated to be 42μs, only about 25% will be left when the ion beam collides with the hydrogen gas. Therefore, the contribution to the cross section by the 4d^{9}5s ^{1}D$_2$ will be limited compared to the other initial Sn^{4+} states.

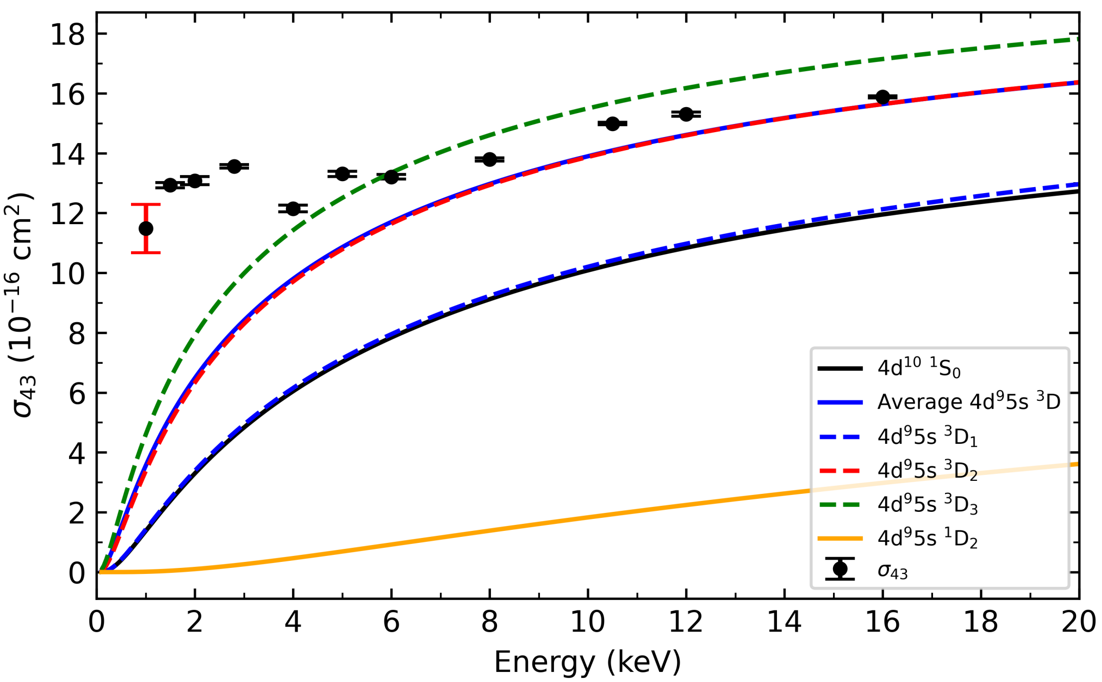

Figure 7.3: Charge transfer cross section for single electron capture determined for a range of projectile energies. The curves indicates multichannel Landau-Zener calculations which were performed for capture from ground state Sn^{4+} as well as several metastable excited Sn^{4+} states. The average cross section of the 4d^{9}5s ^{3}D levels is plotted by averaging over the cross sections based on the total possible states per J-level.

Based on the number of possible states for each 4d^{9}5s ^{3}D level due to their J value, a rough estimation of the abundance of each J-level can be made. The 4d^{9}5s ^{3}D$_1$ has 3 possible states and the 4d^{9}5s ^{3}D$_2$ and 4d^{9}5s ^{3}D$_3$ have 5 and 7 possible states respectively. In total, there are 15 possible states. The abundance for each ion in the 4d^{9}5s ^{3}D levels will then correspond to their number of states divided by 15. In figure 7.3, the average cross section from the Landau-Zener calculations for the 4d^{9}5s ^{3}D states can be seen, based on this abundance. These calculations show good agreement with experimental results. However, the lifetime of the individual 4d^{9}5s ^{3}D states are not taken into account in this calculation. Based on the lifetimes of these excited states, the abundance of the states in the ion beam would likely skew more towards the 4d^{9}5s ^{3}D$_1$ state, due to its very long lifetime. While the Landau-Zener calculations for excited states agree relatively well with the experimental results, this does not necessarily confirm the presence of these states in the ion beam, or their contribution to the determined cross sections. From the Landau-Zener calculations for the excited states, it appears that the electrons are captured in highly excited states of the Sn^{3+} ion. From such highly excited states, auto ionization can readily occur, which is generally a very fast process. In this case, an electron can get captured, but also auto ionize again. During measurements, no charge transfer is measured if this is the case. Therefore, even if these metastable Sn^{4+} ions are present, they might not contribute to single electron capture due to auto ionization.

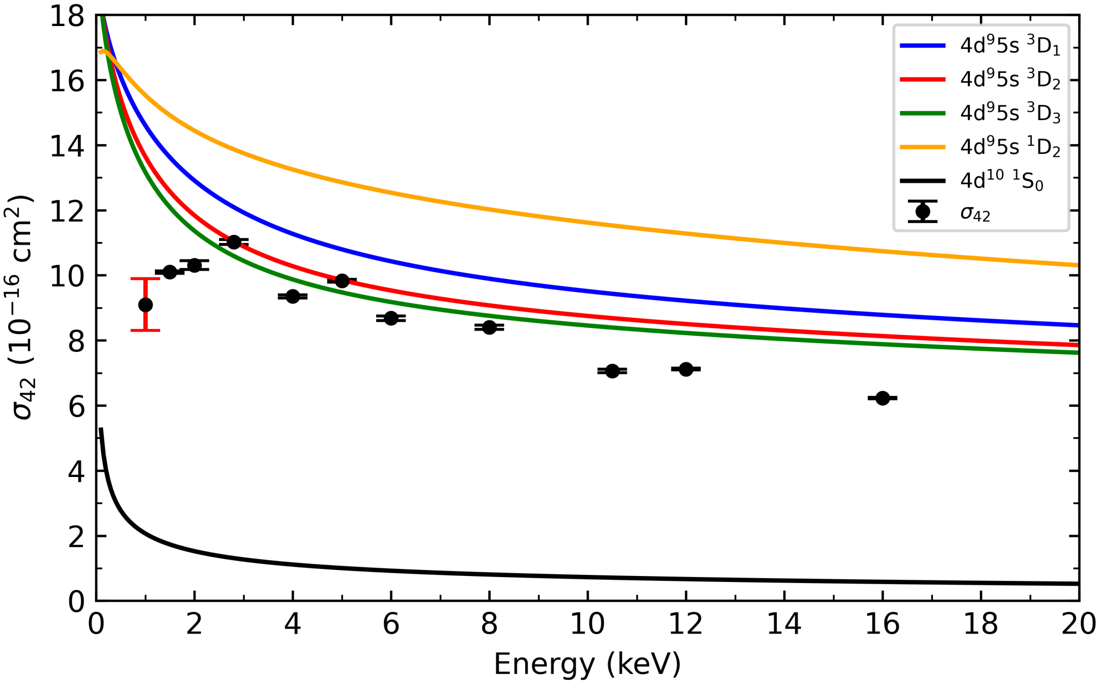

Figure 7.4: Charge transfer cross section for double electron capture experimentally determined for a range of energies. The solid lines indicate multichannel Landau-Zener calculations performed for different initial Sn^{4+} states.

In figure 7.4, experimental values of σ_{42} as well as Landau-Zener calculations for double electron capture can be seen. Double electron capture calculations from the ground state of Sn^{4+} resulted in negligible double capture cross sections, as can be seen in the figure. Additionally, multichannel Landau-Zener calculations were performed for electron capture from the excited Sn^{4+} $4d^95s$ $^3D_3$, $^3D_2$, $^3D_1$ and $4d^95s$ $^1D_2$ states, from which the results are also seen in figure 7.4. For the initial levels of $4d^95s$ ^3D, the calculations were performed for capture into the Sn^{2+} $4d^{10}5s5p$ $^3P_0$, $4d^{10}5s6s$ $^3S_1$, $4d^{10}5s6p$ $^3P_1$, $4d^{10}4f5s$ $^3F_2$, $4d^{10}5s6d$ $^3D_1$ and $4d^{10}5s7p$ $^3P_0$ states. For the initial state $4d^95s$ $^1D_2$, calculations were performed for capture into the $4d^{10}5s5p$ $^1P_1$, $4d^{10}5s6s$ $^1S_0$, $4d^{10}5s5d$ $^1D_2$, $4d^{10}5s6p$ $^1P_1$, $4d^{10}4f5s$ $^1F_3$ and $4d^{10}5s7s$ $^1S_0$ states of Sn^{2+}. The calculated cross sections for double capture from excited states are significantly higher than the calculated cross sections for double capture from the ground state. Also, they show good agreement with the experimental results, assuming that the ion beam consist solely of metastable ions. The calculated cross sections for double capture use a coupling matrix element H_{12}, which was derived for single electron capture processes. Therefore, agreement of data with the Landau-Zener calculations for double capture may also simply be incidental.

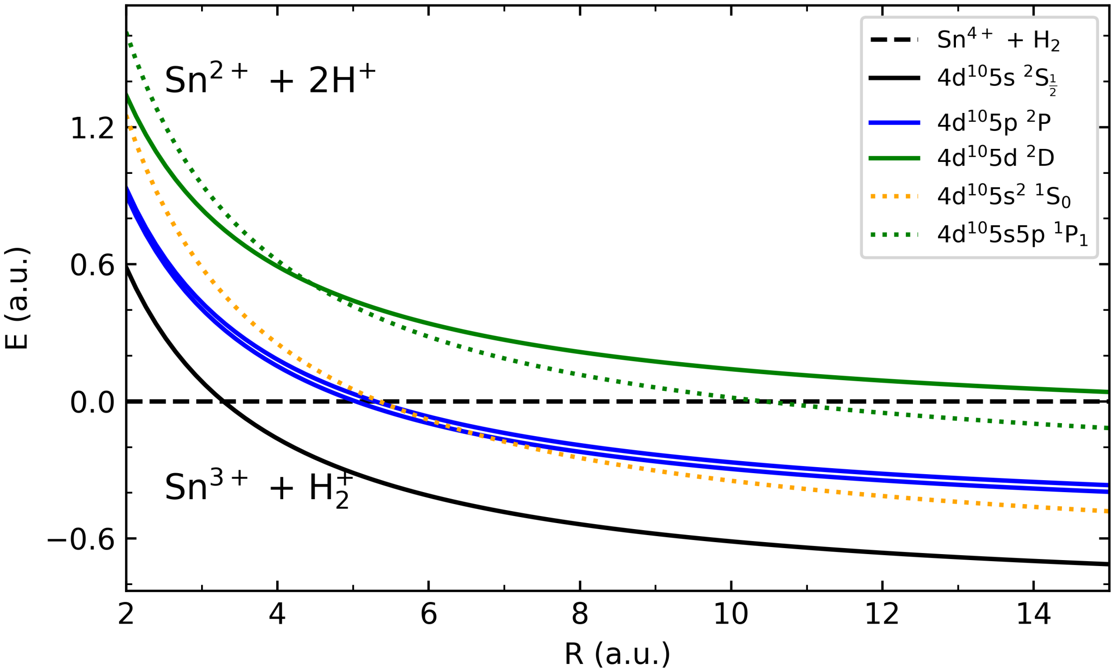

Figure 7.5: Curve crossings for an initial Sn^{4+} + H_2 system with the $Sn^{(3)+}$ + H_2^+ and $Sn^{(2)+}$ + $2H^+$ systems indicated by solid and dotted lines respectively. The curves of the $4d^{10}5p$ ^2P levels of Sn^{3+} and the $4d^{10}5s^2$ state of Sn^{2+} cross at almost the same internuclear distance. In this case, phenomena such as Stuckelberg oscillations can occur, which are oscillations of the system between these energy levels, which complicates accurate Landau-Zener calculations.

In figure 7.5, curve crossings can be seen for different states of Sn^{3+} + H_2^+ and Sn^{2+} + H_2^+ with the initial Sn^{4+} + H_2 system. The solid lines indicate the system where single electron capture has taken place, while the dotted lines indicate the system where double electron capture has taken place. Interestingly, the curves of the $4d^{10}5p$ ^2P levels and the $4d^{10}5s^2$ $^1S_0$ state cross the Sn^{4+} + H_2 system at almost the exact same internuclear distance. In such systems, phenomena such as Stuckelberg oscillations can occur [20], which complicate accurate Landau-Zener calculations even more.

In conclusion, it was found that Landau-Zener calculations for metastable Sn^{4+} ions predict similar cross sections as for the ground state Sn^{4+} ions. If these metastable ion are produced in the ion source, they live long enough to undergo collisions with hydrogen. The Landau-Zener calculations for double capture which were performed in this work are more unreliable, since a coupling matrix element was used which was derived for single electron capture. Additionally, no further corrections for double electron capture were made. Based on the experimental results, no conclusion can be made whether these metastable states are significantly present in the ion beam or not. More measurements are required to identify if a significant amount of metastable Sn^{4+} ions are produced by the ion source. For example, the initial energy of the ion beam can be reduced, such that it takes longer for the ions to travel from the ion source to the collision chamber. By decelerating the ion beam to the same kinetic energy, but for different initial kinetic energies, more metastable ions would have decayed depending on the initial kinetic energy. If a significant amount of metastable ions are present in the ion beam and have an impact on the measured cross sections, differences in cross sections would be present for different initial kinetic energies. If these differences were measured, it would indicate that a significant amount of excited Sn^{4+} ions is present in the ion beam.

8 Conclusion

In this thesis, charge transfer cross sections of Sn^{4+} with molecular hydrogen were experimentally determined. Measurements were performed of determination of ionic populations of tin ions after collisions of Sn^{4+} with molecular hydrogen using a retarding field analyser. The charge transfer cross section were determined in a single collision approximation and subsequently corrected for secondary collisions via an extrapolation to zero pressure. It was found that single electron cross sections are significantly lower for Sn^{4+} ions compared to Sn^{3+} ions. It was found that this is likely due to the difference in availability of energy levels for the electron to be captured into of the Sn^{2+} ion compared to the Sn^{3+} ion. The cross section results were then compared to multichannel calculations from the Landau-Zener model. These calculations were performed for an initial ground state Sn^{4+} ion, but also for the metastable excited Sn^{4+} 4d^{9}5s ^{3}D$_3$, ^{3}D$_2$, ^{3}D$_1$ and 4d^{9}5s ^{1}D$_2$ states. The Landau-Zener calculations for single electron capture for the excited states predict similar cross sections as for groundstate Sn^{4+} ions. Also, the calculations predict that double electron capture is negligible when the projectile is a ground state Sn^{4+} ion, but predicts a significant double capture cross section for the meta stable excited states. However, since the double electron capture calculations use a coupling matrix element derived for single electron capture, the reliability of these calculations can be disputed. Additionally, it was found that the potential energy curves of Sn^{3+} + H$_2^+$ and Sn^{2+} + H$_2^+$ cross the initial Sn^{4+} + H$_2$ system at almost the same internuclear distance, which can give rise to Stuckelberg oscillations, which further complicates accurate Landau-Zener calculations. While it is possible for the metastable ions to be created in the ion source, more measurements are required to determine if a significant amount of these ions are present in the ion beam. Since the measurements were only performed once for each energy, measurements can be repeated to improve the statistical significance of the results. Additionally, the energy range can be expanded to lower projectile energies, since the results suggest that the cross sections start to decrease in this regime. Finally, it might also be possible to find values for cross sections by fitting the complete analytical solutions to data measured at more pressures. In this way, it could be possible to also extract the charge transfer cross sections σ_{32}, σ_{31} and σ_{21}.

9 Acknowledgements

The work done in this thesis was facilitated by the help and support of many people in the quantum interactions and structural dynamics group. First, I would like to thank Ronnie Hoekstra for allowing me to do the research that I did and for his guidance in the process. I would also like to thank Steven Hoekstra for being the second examiner of this thesis. The PhDs in the group also deserve a big thanks. Thank you Klaas, specifically for teaching me how to make and transport an ion beam, as well as for all the help with the Landau-Zener calculations. Thank you Luc, specifically for insights into the experimental setup and the RFA. Thank you Emiel for all the guidance and insights during the measurements and the writing process. I would also like to thank Mart for all his technical support and insights. Without his help, I could not have performed the experiments. I would like to thank everyone in QISD and ARCNL, for making my time during the project very enjoyable. Finally, thank you Stella for your support and for, despite not having physics knowledge, your willingness to read and correct my writing.

References

[1] T. P. Grozdanov, “Classical model for electron capture in collisions of highly charged, fully stripped ions with hydrogen atoms,” *Journal of Physics B: Atomic and Molecular Physics*, vol. 13, p. 3835, oct 1980.

[2] S. Knoop, *Electron Dynamics in Ion-Atom Interactions*. PhD thesis, University of Groningen, 2006.

[3] A. Bárány, G. Astner, H. Cederquist, H. Danared, S. Huldt, P. Hvelplund, A. Johnson, H. Knudsen, L. Liljeby, and K.-G. Rensfelt, “Absolute cross sections for multi-electron processes in low energy Ar^{q+}−Ar collisions: Comparison with theory,” *Nuclear Instruments and Methods in Physics Research Section B: Beam Interactions with Materials and Atoms*, vol. 9, no. 4, pp. 397–399, 1985.

[4] C. Zener, “Non-adiabatic crossing of energy levels,” *Proceedings of the Royal Society of London. Series A, Containing Papers of a Mathematical and Physical Character*, vol. 137, no. 833, pp. 696–702, 1932.

[5] J. F. Ziegler and J. P. Biersack, *The Stopping and Range of Ions in Matter*, pp. 93–129. Boston, MA: Springer US, 1985.

[6] R. E. Olson and A. Salop, “Electron transfer between multicharged ions and neutral species,” *Phys. Rev. A*, vol. 14, pp. 579–585, Aug 1976.

[7] M. Kimura, T. Iwai, Y. Kaneko, N. Kobayashi, A. Matsumoto, S. Ohtani, K. Okuno, S. Takagi, H. Tawara, and S. Tsurubuchi, “Landau-Zener model calculations of one-electron capture from he atoms by highly stripped ions at low energies,” *Journal of the Physical Society of Japan*, vol. 53, no. 7, pp. 2224–2232, 1984.

[8] K. Bijlsma, L. Oltra, E. de Wit, L. Assink, I. Rabadán, L. Méndez, and R. Hoekstra, “Electron capture from molecular hydrogen by metastable Sn^{2+*} ions,” *Atoms*, vol. 12, no. 2, 2024.

[9] H. R. Koslowski and B. A. Huber, “Double-electron capture in low-energy collisions of Ar^{4+} with Ar and Kr,” *Journal of Physics B: Atomic, Molecular and Optical Physics*, vol. 22, p. 2255, jul 1989.

[10] D. Almeida and M. Langford, “Double electron capture in a Landau—Zener model: a reaction window,” *International Journal of Mass Spectrometry and Ion Processes*, vol. 96, no. 3, pp. 331–339, 1990.

[11] S. Buitjes, “Design of a grid-less retarding field analyser for beams of multiply charged sn ions,” 2023.

[12] L. Assink, “In preparation,” 2024.

[13] N. D. Milošević, G. S. Vuković, D. Z. Pavičić, and K. D. Maglić, “Thermal properties of tantalum between 300 and 2300 k,” *International Journal of Thermophysics*, vol. 20, pp. 1129–1136, 06 1999.

[14] S. Rai, K. I. Bijlsma, I. Rabadán, L. Méndez, P. A. J. Wolff, M. Salverda, O. O. Versolato, and R. Hoekstra, “Charge exchange in collisions of 1–100-kev Sn^{3+} ions with H_2 and D_2,” *Phys. Rev. A*, vol. 106, p. 012804, Jul 2022.

[15] R. Hippler, M. Cada, A. Knizek, M. Ferus, and Z. Hubicka, “A pulsed hollow cathode discharge operated in an Ar/N_2/O_2 gas mixture and the formation of nitric oxide,” *Plasma Chemistry and Plasma Processing*, vol. 44, pp. 1053–1068, Mar 2024.

[16] E. de Wit, “Charge exchange in energetic Sn^{q+}-H_2 collisions,” 2023.

[17] N. Singh and A. Goyal, “Energy levels, transition data and collisional excitation cross-section of Sn^{3+} and Sn^{4+} ions,” *Journal of Electron Spectroscopy and Related Phenomena*, vol. 244, p. 146982, 2020.

[18] J. Scheers, A. Ryabtsev, A. Borschevsky, J. C. Berengut, K. Haris, R. Schupp, D. Kurilovich, F. Torretti, A. Bayerle, E. Eliav, W. Ubachs, O. O. Versolato, and R. Hoekstra, “Energy-level structure of Sn^{3+} ions,” *Phys. Rev. A*, vol. 98, p. 062503, Dec 2018.

[19] A. N. Ryabtsev, S. S. Churilov, and É. Y. Kononov, “Autoionizing and highly excited states in the spectrum of triply ionized tin Sn IV,” *Optics and Spectroscopy*, vol. 100, pp. 652–659, May 2006.

[20] O. V. Ivakhnenko, S. N. Shevchenko, and F. Nori, “Nonadiabatic Landau–Zener–Stückelberg–Majorana transitions, dynamics, and interference,” *Physics Reports*, vol. 995, pp. 1–89, 2023.